Investigating Stellar Explosions Using Stellar Evolution Models

Master's thesis submitted in partial fulfillment of the requirements

for the degree of

Masters of Science in Physics

by

Michalis Mastorakis

Under the supervision of

Dr John Antoniadis and Professor Vasiliki Pavlidou

INSTITUTE OF ASTROPHYSICS

Department of Physics
University of Crete
September 28, 2023

Contents

List of Figures 3

List of Tables 4

1 Introduction 5

2 Model 7

2.1 Pre-Explosion Phase 7

2.2 Explosion Phase 10

3 Simulations of Stellar Explosions 14

3.1 Simulations and Population Synthesis 14

3.2 Analysis for all 3 values of Z 15

3.2.1 For $Z = 0.5\ Z_{\odot}$ 16

3.2.2 For $Z = 0.75\ Z_{\odot}$ 19

3.2.3 For $Z = 1.0\ Z_{\odot}$ 22

4 Conclusions 26

5 Acknowledgments 27

6 Bibliography 28

List of Figures

3.1 Histogram of the number of components of the best GMM fitted to the BH mass distribution in each case for all values of Z. . . . 16

3.2 Histograms of two different structural characteristics derived from the statistic 3.2.0.3 of the BH mass distribution for all values of Z. Specifically, 3.2a depicts the number of distinct groups, meaning $D > 4$, found in the distributions. 3.2b depicts the number of large groups, meaning $D > 8$, encountered in the distributions. . . . 17

3.3 Histogram of the number of components of the best GMM fitted to the BH mass distribution in each case for $Z = 0.5\ Z_{\odot}$. . . . 17

3.4 Histograms of two different structural characteristics derived from the statistic 3.2.0.3 of the BH mass distribution for $Z = 0.5\ Z_{\odot}$. Specifically, a depicts the number of distinct groups, meaning $D > 4$, found in the distributions. b depicts the number of large groups, meaning $D > 8$, encountered in the distributions. . . . 18

3.5 Remnant mass distribution a along with the best GMM fit (red line) and BH mass distribution b and along with the best GMM fit for $Z = 0.5$, $\beta = 5.0$, $\alpha_{\text{out}} = 0.3$, $\eta_{\text{out}} = 2.0$, $\zeta = 0.5$, $\alpha_{\text{turb}} = 1.2$, $\tau_{1.5} = 3.0$, $M_{\text{max}} = 2.5$. . . . 18

3.6 Remnant mass distribution a along with the best GMM fit (red line) and BH mass distribution b and along with the best GMM fit for $Z = 0.5$, $\beta = 7.0$, $\alpha_{\text{out}} = 0.3$, $\eta_{\text{out}} = 1.0$, $\zeta = 1.0$, $\alpha_{\text{turb}} = 1.0$, $\tau_{1.5} = 1.8$, $M_{\text{max}} = 2.5$. . . . 19

3.7 Remnant mass M_{grav} - Final mass M_{final} plot for $Z = 0.5$. . . . 20

3.8 Histogram of the number of components of the best GMM fitted to the BH mass distribution in each case for $Z = 0.75\ Z_{\odot}$. . . . 20

3.9 Histograms of two different structural characteristics derived from the statistic 3.2.0.3 of the BH mass distribution for $Z = 0.75\ Z_{\odot}$. Specifically, a depicts the number of distinct groups, meaning $D > 4$, found in the distributions. b depicts the number of large groups, meaning $D > 8$, encountered in the distributions. . . . 21

3.10 Remnant mass distribution a along with the best GMM fit (red line) and BH mass distribution b and along with the best GMM fit for $Z = 0.75$, $\beta = 7.0$, $\alpha_{\text{out}} = 0.5$, $\eta_{\text{out}} = 1.0$, $\zeta = 0.75$, $\alpha_{\text{turb}} = 1.0$, $\tau_{1.5} = 0.6$, $M_{\text{max}} = 2.0$. . . . 21

3.11 Remnant mass distribution a along with the best GMM fit (red line) and BH mass distribution b and along with the best GMM fit for $Z = 0.75$, $\beta = 3.0$, $\alpha_{\text{out}} = 0.3$, $\eta_{\text{out}} = 1.0$, $\zeta = 0.5$, $\alpha_{\text{turb}} = 1.4$, $\tau_{1.5} = 0.6$, $M_{\text{max}} = 2.0$. . . . 22

3.12 Histogram of the number of components of the best GMM fitted to the BH mass distribution in each case for $Z = 1.0\ Z_{\odot}$. . . . 22

3.13 Histograms of two different structural characteristics derived from the statistic 3.2.0.3 of the BH mass distribution for $Z = 1.0\ Z_{\odot}$. Specifically, a depicts the number of distinct groups, meaning $D > 4$, found in the distributions. b depicts the number of large groups, meaning $D > 8$, encountered in the distributions. . . . 23

3.14 Remnant mass distribution a along with the best GMM fit (red line) and BH mass distribution b and along with the best GMM fit for $Z = 1.0$, $\beta = 7.0$, $\alpha_{\text{out}} = 0.3$, $\eta_{\text{out}} = 0.0$, $\zeta = 1.0$, $\alpha_{\text{turb}} = 1.4$, $\tau_{1.5} = 0.6$, $M_{\text{max}} = 3.0$. . . . 24

3.15 Remnant mass distribution a along with the best GMM fit (red line) and BH mass distribution b and along with the best GMM fit for $Z = 1.0$, $\beta = 7.0$, $\alpha_{\text{out}} = 0.3$, $\eta_{\text{out}} = 1.0$, $\zeta = 0.5$, $\alpha_{\text{turb}} = 1.4$, $\tau_{1.5} = 0.6$, $M_{\text{max}} = 2.0$. . . . 24

3.16 Remnant mass M_{grav} - Final mass M_{final} plot for $Z = 1.0$. . . . 25

List of Tables

3.1 Table of the model's parameters that were changed during simulations. 14
3.2 Parameter values for the first example for $Z = 0.5$. 18
3.3 Parameter values for the second example for $Z = 0.5$. 19
3.4 Parameter values for the first example for $Z = 0.75$. 19
3.5 Parameter values for the second example for $Z = 0.75$. 21
3.6 Parameter values for the first example for $Z = 1.0$. 23
3.7 Parameter values for the second example for $Z = 1.0$. 23

Chapter 1

Introduction

The evolution and fate of massive stars are closely connected to numerous unanswered questions in modern astrophysics. These stars play a crucial role in shaping their surroundings through various feedback processes, are the primary source of chemical enrichment throughout the history of the universe, and it is believed that the initial generations of massive stars made significant contributions to the re-ionization of the universe [1]. In the local universe, where heavy elements are more abundant, populations of massive stars exhibit increased diversity [2, 3]. Furthermore, these stars are responsible for the creation of various astrophysical phenomena that we observe [4].

These massive stars release a significant amount of mechanical and radiative energy as well as various heavier elements into their surroundings. These get released through stellar winds over longer periods of time and through supernovae occurring over shorter timescales. As subsequent generations of stars are born, their initial composition becomes enriched with heavy elements synthesized by their predecessors. Understanding how the composition of these stars affects their evolution, energy release, and ultimate fate is crucial for comprehending the evolution of galaxies, as well as the characteristics of stellar populations, astrophysical events such as supernovae [4], and the merging of compact objects [5] throughout the history of the universe.

Towards the end of their life, massive stars have the potential to undergo explosive events known as core-collapse supernovae (CCSNe). These explosions may result in the formation of either a neutron star (NS) or a black hole (BH) remnant. In some cases, massive stars may collapse directly, without producing an explosion, to form a BH. In other cases, very massive stars experience pair instability SNe, causing them to explode without leaving any remnants [6].

Most massive stars are considered to be constituents of binary or multiple systems which leads to interactions via mass transfer [7, 8, 9, 10]. This kind of binary interaction may result in the (partial) removal of the hydrogen-rich envelope of the star [11, 12, 13, 14, 15, 16, 17, 18], thus leaving behind a stripped-envelope star. Such stars differ greatly from their hydrogen-rich counterparts in their observational properties, their evolution and their remnants.

One of the pending problems in stellar astrophysics is the connection between the properties of the CCSNe progenitors and the properties of the resulting explosion and the compact remnant. This difficulty arises from the fact that a systematic study from first principles is extremely difficult as the CCSNe explosion mechanism is not yet fully understood [19, 20]. Several attempts have been made in order to understand the CCSNe mechanism from first-principle CCSNe simulations using numerous techniques [21, 22, 23, 24, 25, 26]. None achieve their goal fully mainly due to the computational cost and difficulty of scanning the whole parameter space of progenitor models in zero-age main sequence (ZAMS) mass, metallicity and rotation rate using 3D simulations.

But not all hope is lost, as we can gain insight into the CCSNe mechanism by using approximate analytic models or parameterised simulations. We will be using the one proposed by Müller et al. [27]. In their model, they split the evolution in two phases, the pre-explosion phase, where analytic predictions for the heating conditions can be made, and the final explosion and remnant properties that can be described using simple ordinary differential equations (ODEs). One benefit of this approach is that it allows for rapid estimation of explosion characteristics using solely the stellar structure during the initial stages of collapse as input.

With the rise of gravitational wave (GW) astronomy, a new window to study the universe has opened. With the detection of almost 100 GW mergers, the NS and BH mass distribution is being unveiled across cosmic time. Given the information being provided to us, it is as good a time as it gets to try and understand better the pre-SN evolution of massive stars in order to probe the distribution of remnant (NS and BH) masses. This will help us understand better the formation of highly asymmetric mergers observed during the observation runs. For example, GW 190814 [28] is a gravitational wave merger of a $(23 \pm 1)\ M_\odot$ BH with a $(2.6 \pm 0.1)\ M_\odot$ compact object of unknown nature.

Understanding the mechanism behind the formation of NSs and BHs can help one study better GW mergers, peculiar in nature or not. In order to probe this mechanism, which is the focus of this project, we will use the model of Müller et al. [27] (as mentioned before). As input we will use profiles of stripped-envelope stars in the range from $4.5 - 70\ M_\odot$, with a 0.5 step increment, produced using the Modules-for-Experiments-in-Stellar-Astrophysics (MESA)

code [29, 30, 31, 32, 33] for 3 values of metallicity, 0.5, 0.75 and 1.0 times the solar metallicity $Z_{\odot}$ [34, 35]. This model depends on 7 parameters that govern the underlying physical processes of the system. We perform an extensive parameter study using the value ranges given in literature for each parameter. In each instance, after getting the estimated data for the explosion (if it happened) and the remnant, we performed a population synthesis in order to get a remnant mass distribution.

Chapter 2

Model

As mentioned in the previous section, the model we will use is the one proposed by Müller et al. [27]. In order to spare you the reading of the whole paper, we shall explain here the model in a simpler manner. We will present it here as it is in the paper, namely in two parts: 1) the pre-explosion phase and 2) the explosion phase. Before that, let us describe briefly the different phases of the CCSNe evolution process in order to highlight the physical processes that the model needs to capture.

During the core-collapse, the iron core of the massive star collapses into a NS which is accompanied by the core bounce that leads to the creation of a shock wave inside the gas. After that, the shock rapidly stalls due to the photodisintegration of heavy nuclei and neutrino losses. However, even if the shock has stalled, there is a bit of an expansion for some milliseconds due to matter being piled onto the proto-NS. Following that, we have a phase where the entire post-shock region is cooled and after that, a region of net neutrino heating (which is called the gain region) appears. This period is the pre-explosion phase.

After that, the shock radius reaches its maximum and then proceed to recede again. At this time, we expect shock revival by a neutrino-driven mechanism to take place. This occurs when the accreted material spend sufficient time in the gain region which provides the material with enough energy that originates from neutrinos to counteract its binding energy. This marks the start of the explosion phase.

2.1 Pre-Explosion Phase

During this phase, the gain region is modeled as an adiabatically stratified layer that is dominated by radiation pressure ($P \propto T^4$), meaning the pressure P, density ρ, and temperature T can be described approximately by power laws

$$P \propto r^{-4},\ \rho \propto r^{-3},\ T \propto r^{-1} \tag{2.1.0.1}$$

Furthermore, it is assumed that the matter reaches the NS within a constant multiple of the free-fall timescale (τ_{ff}) for a given mass shell (a mass shell being a sphere that constrains mass M, so it is described by its mass coordinate M). The infall time of a infalling mass shell of mass M is

$$t = C\tau_{\text{ff}} = \sqrt{\frac{\pi}{4G\overline{\rho}}} \tag{2.1.0.2}$$

where

$$\overline{\rho} = \frac{3M}{4\pi r^3} \tag{2.1.0.3}$$

is the average density of a given mass shell that is located at an initial radius r. Then, with the result from [36] we can calculate the accretion rate as

$$\dot{M} = \frac{2M}{t}\frac{\rho}{\overline{\rho} - \rho} \tag{2.1.0.4}$$

where ρ is the initial density of the given mass shel prior to collapse. The dimensionless constant in eq. 2.1.0.2 has been chosen such that the analytic estimates match the results from numerical simulations in the late accretion phase.

In the pre-explosion phase, it can be assumed that the shock is quasi-stationary, meaning that the shock velocity is negligible. So, by using the strong-shock approximation and neglecting the thermal pressure in the pre-shock region, one can write the Rankine-Hugoniot conditions that define the post-shock density ρ_{sh} and pressure P_{sh} as

$$\rho_{\text{sh}} = \beta\rho_{\text{pre}} \tag{2.1.0.5}$$

and

$$P_{\text{sh}} = \frac{\beta - 1}{\beta}\rho_{\text{pre}}v_{\text{pre}}^2 \tag{2.1.0.6}$$

where $\rho_{\rm sh}$ and $v_{\rm pre}$ are the pre-shock density and velocity respectively, and β is the compression rate at the shock. Many simulations have shown that $v_{\rm pre}$ reaches a large fraction of the free-fall velocity, and so one can use

$$v_{\rm pre} = \sqrt{\frac{2GM}{r_{\rm sh}}} \tag{2.1.0.7}$$

The pre-shock density can be calculated from the mass accretion rate (assuming that the pre-shock density is constant) as

$$\rho_{\rm pre} = \frac{\dot{M}}{4\pi r^2 v_{\rm pre}} \tag{2.1.0.8}$$

The formulation of an inner boundary condition for the gain region is necessary. In order to be able to formulate such a thing, we need a model that describes the evolution of the gain region radius $r_{\rm g}$, the neutrino luminosity L_ν, and the mean energy of the electron neutrinos and anti-neutrinos E_ν as a function of time, proto-NS mass and accretion rate. To start with, in [37] they show that

$$E_\nu \propto M \tag{2.1.0.9}$$

and since the cooling layer is taken to be approximately isothermal, it also holds that

$$T_g \propto M \tag{2.1.0.10}$$

Then, in order to find the gain radius $r_{\rm g}$ one need only follow what is said in [20]. There, they note that the accreted matter loses approximately half of its gravitational potential energy as accretion luminosity $GM\dot{M}/(2r_{\rm g})$ close to the gain region, and by equating this contribution in the luminosity to the grey-body luminosity at the gain radius it arises that

$$E_\nu^4 r_{\rm g}^2 \propto T_{\rm g}^4 r_{\rm g}^2 \propto M^4 r_{\rm g}^2 \propto \frac{GM\dot{M}}{2r_{\rm g}} \tag{2.1.0.11}$$

which gives

$$r_{\rm g} \propto \frac{\dot{M}^{1/3}}{M} \tag{2.1.0.12}$$

However, for small $\dot{M}$ this breaks down, and one must use a smooth interpolation between this and the cold NS radius r_0 as

$$r_{\rm g} = \left[r_1^3 \left(\frac{\dot{M}}{M_\odot s^{-1}} \right) \left(\frac{M}{M_\odot} \right)^{-3} + r_0^3 \right]^{1/3} \tag{2.1.0.13}$$

where $r_0 = 12$ km and $r_1 = 120$ km.

The neutrino (both anti- and normal- neutrinos are considered together in this model) luminosity is taken to consist of two components, the first being the accretion luminosity $L_{\rm acc}$

$$L_{\rm acc} = \zeta \frac{GM\dot{M}}{2r_{\rm g}} \tag{2.1.0.14}$$

where ζ is an efficiency parameter that gauges the efficiency, and the second being the diffusive luminosity $L_{\rm diff}$ that originates from the deeper layers of the proto-NS. Now, in order to estimate $L_{\rm diff}$ we will make use of the findings of [38, 39] which enable us to assume that the binding energy of a cold NS, given by

$$E_{\rm bind} \approx 0.084\ M_\odot c^2 \left(\frac{M_{\rm NS}}{M_\odot} \right)^2 \tag{2.1.0.15}$$

is radiated away as diffusion luminosity over a timescale $\tau_{\rm cool}$, where $M_{\rm NS}$ is the gravitational mass of the NS. In order to account for the fact that the diffusion timescale is increased by higher densities, temperatures and chemical potentials (for electron neutrinos) in high mass NS, an additional power-law dependence on the baryonic NS mass has to be introduced in $\tau_{\rm cool}$, thus

$$\tau_{\rm cool} = \tau_{1.5} \times \left(\frac{M}{1.5\ M_\odot} \right)^{5/3} \tag{2.1.0.16}$$

where $\tau_{1.5}$ is the cooling timescale of a 1.5 $M_\odot$ mass NS. With that in mind, we can define the (anti-)neutrino luminosity as

$$L_\nu = -0.3\dot{E}_{\rm bind} \approx 0.3 \times \frac{e_{\rm bind}(M)}{\tau_{\rm cool}(M)} \tag{2.1.0.17}$$

where the factor 0.3 accounts for the fact that about only one third of the binding energy is emitted in the form of L_ν that contributes to the neutrino heating in the gain region. If on the other hand we neglect the secular changes in M and $\tau_{\rm cool}$, the diffusion luminosity can be defined as

$$L_{\rm diff} = E_{\rm bind}(M) e^{-t/\tau_{\rm cool}(M)} \tag{2.1.0.18}$$

where this is used as an instantaneous estimation for $L_{\rm diff}$ at constant M, and we have defined the binding energy in terms of the baryonic mass instead of the gravitational, which is given by

$$E_{\rm bind} = \left(M - \frac{\left(-1 + \sqrt{1 + 0.336\ M/M_\odot}\right) M_\odot}{0.168} \right) c^2 \tag{2.1.0.19}$$

In order to account for general relativistic effects on the neutrinos that originate close from the proto-NS, meaning

$$L_\nu = \sqrt{1 - \frac{2GM}{c^2 r_{\rm PNS}}} (L_{\rm acc} + L_{\rm diff}) \tag{2.1.0.20}$$

where the radius of the proto-NS is taken to be $r_{\rm PNS} \approx 5/7\ r_{\rm g}$.

As soon as the gain radius, mean neutrino energy and neutrino luminosity are calculated, we can start conceiving the second (inner) boundary conditions for the pressure stratification in the gain region. If we take the neutrino heating and the cooling rate per unit mass to be at an equilibrium at the gain radius, we have for the temperature at the gain region

$$T_{\rm g}^6 \propto \frac{L_\nu E_\nu^2}{r_{\rm g}^2} \tag{2.1.0.21}$$

Since $P_g \propto T_{\rm g}^4$ (since we talk about neutrinos which can be modeled as a relativistic gas), we get that the pressure at the gain region scales as

$$P_g^{3/2} \propto \frac{L_\nu E_\nu^2}{r_{\rm g}^2} \tag{2.1.0.22}$$

and this formulates the second (inner) boundary condition for the pressure.

In order to find the shock radius, we must solve eqs. 2.1.0.6, 2.1.0.22 together with $P \propto r^{-4}$, which yields

$$r_{\rm sh} \propto \frac{\left(L_\nu E_\nu^2\right)^{4/9} r_{\rm g}^{16/9}}{\dot{M}^{2/3} M^{1/3}} \propto \frac{L_\nu^{4/9} M^{5/9} r_{\rm g}^{16/9}}{\dot{M}^{2/3}} \tag{2.1.0.23}$$

where the second form is obtained by means of eq. 2.1.0.9. In [40], the authors suggest a modification of the shock radius to account for the multi-dimensional (multi-D) effects that may affect the shock radius but are not considered in a 1-dimensional study. To such extend, they modify simply the shock radius as

$$r_{\rm sh} \to r_{\rm sh} \left(1 + \frac{4 \left\langle {\rm Ma}^2 \right\rangle}{3} \right)^{2/3} \tag{2.1.0.24}$$

where Ma is the Mach number. Despite its simplicity, it works remarkably well as it has been showed by [25]. Since the shock radius' only use is to find the point in time when the critical explosion condition $\tau_{\rm adv}/\tau_{\rm heat} = 1$ is met, the turbulent Mach number can be replaced by its critical value $\left\langle {\rm Ma}^2 \right\rangle \approx 0.4649$ (as found in [40]), which implies that eq. 2.1.0.24 can be written in the simpler form

$$r_{\rm sh} \to \alpha_{\rm turb} r_{\rm sh} \tag{2.1.0.25}$$

where $\alpha_{\rm turb}$ is a constant factor that accounts for the turbulent effects. By taking all the above into account, the final scaling law for the shock radius is

$$r_{\rm sh} = \alpha_{\rm turb} \times 55\ {\rm km}\ \times \left(\frac{L_\nu}{10^{52}\ {\rm erg}\ s^{-1}} \right)^{4/9} \times \left(\frac{M}{M_\odot} \right)^{5/9} \times \left(\frac{r_{\rm g}}{10\ {\rm km}} \right)^{16/9} \times \left(\frac{\dot{M}}{M_\odot s^{-1}} \right)^{-2/3} \tag{2.1.0.26}$$

Now that we have an expression for the shock radius, a scaling law for the advection timescale can be found easily as

$$\tau_{\rm adv} = \frac{M_{\rm g}}{\dot{M}} = \frac{1}{\dot{M}} \int_{r_{\rm g}}^{r_{\rm sh}} dr\ 4\pi r^2 \beta \rho_{\rm pre} \left(r_{\rm sh}/r\right)^3 \approx 18\ {\rm ms}\ \times \left(\frac{r_{\rm sh}}{100\ {\rm km}} \right)^{3/2} \left(\frac{M}{M_\odot} \right)^{-1/2} \ln \frac{r_{\rm sh}}{r_{\rm g}} \tag{2.1.0.27}$$

where this expression fits the results of [40]. In order to define an expression for the heating timescale $\tau_{\rm heat}$ we need the average mass-specific neutrino heating rate $\dot{q}_\nu$ and the average net binding energy (i.e. thermal, kinetic and potential energy) $e_{\rm g}$ of matter in the gain region. The scaling law of $\dot{q}_\nu$ can be found using the results of [20, 40] to be

$$\dot{q}_\nu \propto \frac{L_\nu E_\nu^2}{r_{\rm g}^2} \tag{2.1.0.28}$$

The process to find the average binding energy is not an easy one because neither assuming a constant time-independent binding energy as in [40] nor the assumption that $e_{\rm g}$ scales with the gravitational potential at the shock as in [20] conform with the results from simulations. So, in order to get a better estimate for $e_{\rm g}$, Bernoulli's theorem for a

stationary compressible flow in spherical symmetry [41] must be invoked. The sum of the total enthalpy h (which includes the rest mass contributions), the kinetic energy density, and the gravitational potential are conserved during the infall process, we can attribute to the sum its initial and negligibly small value at the initial position of a given mass shell

$$h + \frac{1}{2}\rho v^2 + \Phi = 0 \tag{2.1.0.29}$$

If we neglect the kinetic energy in the post-shock region, we have

$$\epsilon_{\rm therm} + \epsilon_{\rm diss} + \frac{P_{\rm sh}}{\rho_{\rm sh}} - \frac{GM}{r_{\rm sh}} \approx 0 \tag{2.1.0.30}$$

which gives us the thermal energy $\epsilon_{\rm therm}$ per unit mass just behind the shock. We have to note here that the rest mass contributions in eq. 2.1.0.30 are excluded from $\epsilon_{\rm therm}$ and is absorbed by the dissociation energy $\epsilon_{\rm diss}$ term. Since in the post-shock region radiation pressure dominates, we have

$$\frac{P_{\rm sh}}{\rho_{\rm sh}} = \frac{\epsilon_{\rm therm}}{3} \tag{2.1.0.31}$$

and hence we get

$$\frac{4}{3}\epsilon_{\rm therm} + \epsilon_{\rm diss} = \frac{GM}{r_{\rm sh}} \Rightarrow \epsilon_{\rm therm} = \frac{3}{4}\left(\frac{GM}{r_{\rm sh}} - \epsilon_{\rm diff}\right) \tag{2.1.0.32}$$

With this expression for the thermal energy per unit mass, we get that the post-shock binding energy without rest mass contributions is

$$|e_{\rm g}| = \left|\epsilon_{\rm therm} - \frac{GM}{r_{\rm sh}}\right| = \frac{3}{4}\epsilon_{\rm diss} + \frac{GM}{4r_{\rm sh}} \tag{2.1.0.33}$$

If we assume total dissociation of the infalling matter into nucleons, we get for the dissociation energy $\epsilon_{\rm diss} \approx 8.8$ MeV. Let us note here that the value of the total energy per unit mass immediately behind the shock is used as a proxy for the entire gain region. We can now combine eqs. 2.1.0.28 and 2.1.0.33 and by choosing the appropriate proportionality constant to abide to simulations, we get the following expression for the heating timescale

$$\tau_{\rm heat} = 150 \text{ ms} \times \left(\frac{|e_{\rm g}|}{10^{19} \text{ erg } s^{-1}}\right) \times \left(\frac{r_{\rm g}}{100 \text{ km}}\right) \times \left(\frac{L_\nu}{10^{52} \text{ erg } s^{-1}}\right) \times \left(\frac{M}{M_\odot}\right)^{-2} \tag{2.1.0.34}$$

From eqs. 2.1.0.26, 2.1.0.27 and **??** we can infer the mass in the gain region $M_{\rm g}$, the average neutrino heating rate per unit mass $\dot{q}_\nu$ and the volume-integrated neutrino heating rate $\dot{Q}_\nu = \dot{q}_\nu M_{\rm g}$, which enable us to define the efficiency parameter $\eta_{\rm acc}$ as

$$\eta_{\rm acc} = \frac{\dot{Q}_\nu}{\dot{M}} \tag{2.1.0.35}$$

which will be useful for the treatment of the next part, the explosion phase.

2.2 Explosion Phase

With the procedure we described in the previous section we can compute the critical timescale ratio $\tau_{\rm adv}/\tau_{\rm heat}$ as a function of the mass coordinate of the infalling shells. With this ratio we can deduce the remnant of the stellar model as follows: If we find the ratio to be < 1 throughout the star or at least for all M smaller than the maximum baryonic NS mass $M_{\rm max}$ (which is a parameter in the model and thus does not have a predetermined value), then the star is taken to result in a BH without ever experiencing shock revival. On the other hand, if no such criterion for the ratio is satisfied, then we consider the minimum M for which the ratio satisfies $\tau_{\rm adv}/\tau_{\rm heat} = 1$ as an "initial mass cut" $M_{\rm ini}$ and then begin the process of estimating the residual accretion onto the proto-NS and the explosion parameters. This is done by relating the amount of accretion after shock revival, the shock propagation, and the energetics of the incipient explosions (which is quantified by the diagnostic explosion energy $E_{\rm diag}$, which in other words is the total energy of the material that is nominally unbound at a given stage after shock revival) to each other. Let us now see how this is achieved.

Except for the least massive SN progenitors [42, 43], simulations of SN explosions from first principles [44, 45, 26, 46] (and many more) have shown that the accretion downflows persist for many hundreds of milliseconds after shock revival, and in many cases it persists till the end of the simulations which makes the final explosion parameters of the model difficult to determine. In [41] a more quantitative analysis of the mass fluxes $\dot{M}_{\rm out}$ and $\dot{M}_{\rm acc}$, where the former refers to neutrino-driven outflows and the latter to cold accretion downflows, showed that the accretion by downflows outweighs the outflow rate for a long time,

$$\dot{M}_{\rm acc} \gg \dot{M}_{\rm out} \tag{2.2.0.1}$$

This long persistence of accretion posses a major technical problem for simulations. However, it helps in simplifying the treatment of the post-explosion phase by allowing us to use the same estimates for the accretion rate onto the

proto-NS (and consequently for the NS contraction, the neutrino luminosity and the neutrino heating rate) as in the pre-explosion phase (see Section 2.1). So, in the initial phase of the explosion (which will be called **phase I** hereafter for simplicity) the primary contribution to the explosion are the neutrino-heated outflow that are driven by relatively high accretion luminosity.

In time, the residual accretion will cease and eq. 2.2.0.1 will break down. This indicates the start of the cooling period of the proto-NS as it radiates neutrinos over a timescale of several seconds and this neutrino driven wind will contribute to the explosion energy. This period will be called **phase II** hereafter.

In [47] they propose a way to estimate the transition between phase I and phase II. The transition happens approximately when the newly shocked material is accelerated to the local escape velocity as this prevents accretion onto the proto-NS on a short timescale (however the interaction with the rest of the ejecta may lead to late-time fallback). This process can be translated into a condition for the shock velocity: Since at the transition point the shock will have propagated to several thousands or even tens of thousands of kilometers, the post-shock velocity in the immediate vicinity will be high compared to the small pre-shock infall velocity. So, if the pre-shock velocity is negligible, we can define the post-shock velocity v_{post} of the newly shocked material in terms of the pre-shock velocity v_{sh} and the compression ratio β_{expl} as

$$v_{\mathrm{post}} = \frac{\beta_{\mathrm{expl}} - 1}{\beta_{\mathrm{expl}}} v_{\mathrm{sh}} \tag{2.2.0.2}$$

and thus the accretion criterion can be expressed simply as

$$\frac{\beta_{\mathrm{expl}} - 1}{\beta_{\mathrm{expl}}} v_{\mathrm{sh}} = \sqrt{\frac{2GM}{r}} \tag{2.2.0.3}$$

where r is the initial radius of the mass shell M and is assumed that it has not moved that far from its initial position when it is hit by the shock. It is assumed that accretion will subside when the criterion in eq. 2.2.0.3 is met. It is important to note here that the compression ratio β_{expl} at the explosion phase is different and will be smaller in general than the pre-explosion compression ratio $\beta = (\gamma + 1)/(\gamma - 1)$ for an ideal gas with a γ-law equation of state (EoS) due to the nuclear burning in the shock.

How the shock propagates depends greatly on the energetics of the underlying explosion. Specifically, in [41] it is highlighted that the enormously complicated mutli-D flow structure after shock revival does not affect greatly the shock velocity as the average shock velocity (defined simply as the time derivative of the average shock radius) does not deviate much from the analytic formula given in [48] where they consider shock propagation in spherical symmetry

$$v_{\mathrm{sh}} = 0.794 \left(\frac{E_{\mathrm{diag}}}{M - M_{\mathrm{ini}}} \right)^{1/2} \left(\frac{M - M_{\mathrm{ini}}}{\rho r^3} \right)^{0.19} \tag{2.2.0.4}$$

where E_{diag} is the diagnostic explosion energy as we defined it previously, and ρ, r refer to the initial progenitor model.

Both the final explosion energy and the final NS mass (which can be found through the amount of residual accretion) can be calculated using eqs. 2.2.0.3 and 2.2.0.4 by simply considering a model for the evolution of E_{diag} in phase I and II. During phase I, the explosion energy mainly consists of strong neutrino heating that is powered by the accretion downflows and the nuclear burning that takes place in the shock. This together with the results of simulations enable us to estimate the contribution of the neutrino heating as follows: As the outflowing material just barely reaches positive total energy, the outflow rate is roughly given by the ratio of the volume-integrated neutrino heating rate $\dot{Q}_\nu$ and the initial binding energy at the gain radius $|e_{\mathrm{g}}|$

$$\dot{M}_{\mathrm{out}} = \frac{\eta_{\mathrm{out}} \dot{Q}_\nu}{|e_{\mathrm{g}}|} = \frac{\eta_{\mathrm{out}} \eta_{\mathrm{acc}} \dot{M}_{\mathrm{acc}}}{|e_{\mathrm{g}}|} \tag{2.2.0.5}$$

where η_{out} is a dimensionless parameter that gauges the efficiency of the conversion of neutrino heating to an outflow rate, and we used the heating from eq. 2.1.0.35 that we calculated in Section 2.1 since the accretion onto the proto-NS (and hence the neutrino heating rate) are barely affected by the initial outflows. Let us mention here that η_{out} must not be confused with the α_{out} parameter that shall be introduced later and expresses the surface fraction that is occupied by neutrino-driven outflows far away from the gain radius. [49, 50] show that the energy input via neutrino heating into the outflow is used solely to completely unbind the material and the energy contribution arises from the recombination of nucleons. With that, the evolution of the diagnostic explosion energy is

$$\dot{E}_{\mathrm{diag}} = \epsilon_{\mathrm{rec}} \dot{M}_{\mathrm{out}} \tag{2.2.0.6}$$

where ϵ_{rec} is the recombination energy. The value of the recombination energy depends on what kind of particles are created by the nuclear burning and the turbulent interaction between downflows and outflows. For this model, the value $\epsilon_{\mathrm{rec}} \approx 5$ MeV is used as found by [41].

Instead of eq. 2.2.0.6, it is more useful to express it in terms of derivatives of the mass coordinate M_{sh} that is reached at a given time by the shock, meaning we will find an expression for $dE_{diag}/dM_{\mathrm{sh}}$. If we assume that a fraction

$(a - \alpha_{\rm out})$, where $\alpha_{\rm out}$ is the already mentioned surface fraction that is occupied by neutrino-driven outflows, of the shocked mass is accreted in the end, then $E_{\rm diag}$ should grow as

$$\frac{dE_{diag}}{dM_{\rm sh}} = \epsilon_{\rm rec}\frac{dM_{out}}{dM_{\rm acc}}\frac{dM_{\rm acc}}{dM_{\rm sh}} = \frac{(1-\alpha_{\rm out})\epsilon_{\rm rec}\eta_{\rm out}\eta_{\rm acc}}{|e_{\rm g}|} \tag{2.2.0.7}$$

where the term $dM_{out}/dM_{\rm acc}$ can be calculated from eq. 2.2.0.5, and the term $dM_{\rm acc}/dM_{\rm sh}$ is simply the accreted fraction $(1-\alpha_{\rm out})$. Eq. (2.2.0.7) gives us the eventual contribution to the explosion energy form a given mass shell. However, the diagnostic explosion energy will be lower at the time when the mass shell is shocked. This lower value is needed in order to determine when accretion subsides (which is done via the post-shock velocity). In order to calculate the diagnostic energy $E_{\rm imm}$ at the time when the shock reaches a given mass shell, we first assume that the accretion rate is given by eq. 2.2.0.1. As we have already said in Section 2.1, the shock sweeps up matter at a rate of

$$\frac{dM_{\rm sh}}{dt} = 4\pi r^2 v_{\rm sh}\rho \tag{2.2.0.8}$$

and so, for the evolution of the diagnostic explosion energy when the shock reaches a given mass shell we get

$$\frac{dE_{\rm imm}}{dM_{\rm sh}} = \frac{dE_{\rm imm}}{dt}\frac{dt}{dM_{\rm sh}} = \frac{1}{4\pi r^2 v_{\rm sh}\rho}\frac{dE_{diag}}{dt} = \frac{1}{4\pi r^2 v_{\rm sh}\rho}\frac{\epsilon_{\rm rec}\dot{Q}_\nu}{|e_{\rm g}|} = \frac{\epsilon_{\rm rec}\eta_{\rm out}\eta_{\rm acc}\dot{M}}{4\pi r^2 v_{\rm sh}\rho|e_{\rm g}|} \tag{2.2.0.9}$$

where since $E_{\rm imm}$ is nothing more than $E_{\rm diag}$ just when the shock has reached a given masss shell. Eq. 2.2.0.9 holds in the regime where the $v_{\rm sh} \gg v_{\rm pre}$ (in case one has forgotten what this symbols mean, the condition that the above equation holds is when the shock velocity $v_{\rm sh}$ is substantially larger than the pre-shock infall velocity $v_{\rm pre}$). However, right after shock revival that does not hold, and it can instead be assumed that the shocked matter is accreted onto the proto-NS. To account for both regimes, the equation for the growth of $E_{\rm imm}$ must become

$$\frac{dE_{\rm imm}}{dM_{\rm sh}} = \frac{\epsilon_{\rm rec}\eta_{\rm acc}\eta_{\rm out}}{|e_{\rm g}|}\min\left(1, \frac{\dot{M}}{4\pi r^2 v_{\rm sh}\rho}\right) \tag{2.2.0.10}$$

Once we can calculate $E_{\rm imm}$, we can find the shock velocity from eq. 2.2.0.4 and then determine the amount of explosive burning as we will see now.

Excluding the energy input by neutrino heating, it must also account for the fact that provided the post-shock temperatures are high enough, a contribution to the explosion energy must be considered to account for the initially bound shocked material and the nuclear burning that takes place in the shock. The correction to the growth rate is easily done by adding two terms, one corresponding to the binding energy per unit mass $\epsilon_{\rm bind}$ and one for the nuclear burning $\epsilon_{\rm burn}$ as

$$\frac{dE_{diag}}{dM_{\rm sh}} = \frac{(1-\alpha_{\rm out})\epsilon_{\rm rec}\eta_{\rm out}\eta_{\rm acc}}{|e_{\rm g}|} + \alpha_{\rm out}(\epsilon_{\rm bind} + \epsilon_{\rm burn}) \tag{2.2.0.11}$$

As opposed to neutrino heating powered by accretion, $\epsilon_{\rm bind}$ and $\epsilon_{\rm burn}$ contribute to the energy instantly, so eq. 2.2.0.10 becomes after the corrections

$$\frac{dE_{\rm imm}}{dM_{\rm sh}} = \frac{\epsilon_{\rm rec}\eta_{\rm out}\eta_{\rm acc}}{|e_{\rm g}|}\min\left(1, \frac{\dot{M}}{4\pi r^2 v_{\rm sh}\rho}\right) + \alpha_{\rm out}(\epsilon_{\rm bind} + \epsilon_{\rm burn}) \tag{2.2.0.12}$$

It is noteworthy that both $\epsilon_{\rm bind}$ and $\epsilon_{\rm burn}$ are multiplied by $\alpha_{\rm out}$ as not all the shocked material gets swept up by the ejecta, some is channelled into downflows.

We can define $\epsilon_{\rm burn}$ in terms of the initial and final mass fractions X_i and X_i' prior to and after nuclear burning respectively, and the rest-mass contributions $\epsilon_{\rm rm}$ per unit mass for a nucleus i as

$$\epsilon_{\rm burn} = \sum_i (X_i - X_i')\,\epsilon_{{\rm rm},i} \tag{2.2.0.13}$$

So, in order to proceed we need knowledge about X_i. To do so, we shall employ the "flashing" method as in [51] where they assume that the different burning processes take place instantaneously when the different temperatures required for their ignition are satisfied. With that, it is possible to calculate the post-shock temperature $T_{\rm sh}$ if we simply assume that the pressure in the domain behind the shock is dominated by radiation pressure and that the infall velocity is negligible compared to the shock velocity. Under these assumptions, the post-shock pressure $P_{\rm sh}$ can be found using the jump conditions and we find

$$P_{\rm sh} = \frac{\alpha T_{\rm sh}^4}{3} = \frac{\beta_{\rm expl} - 1}{\beta_{\rm expl}}\rho v_{\rm sh}^2 \tag{2.2.0.14}$$

or, solving for $T_{\rm sh}$

$$T_{\rm sh} = \left(\frac{3\beta_{\rm expl} - 1}{\alpha\beta_{\rm expl}}\rho v_{\rm sh}^2\right)^{1/4} \tag{2.2.0.15}$$

where α is the radiation constant.

The initial conditions depend on $T_{\rm sh}$ greatly and change as follows:

(*i*) For 2.5×10^9 K $\leq T_{\rm sh} \leq 3.5 \times 10^9$ K, elements lighter than O are burnt to ^{16}O.

(*ii*) For 3.5×10^9 K $\leq T_{\rm sh} \leq 5 \times 10^9$ K, elements lighter than Si are burnt to ^{28}Si.

(*iii*) For 5×10^9 K $\leq T_{\rm sh} \leq T_\alpha$, everything burns to ^{56}Ni by following [52] where the threshold temperature for complete Si is different from [51].

T_α denotes the density-dependent temperature for which the mass fraction of $\alpha-$particles reaches 0.5 in nuclear statistical equilibrium. From [53, 51] we get that T_α is given by

$$\log_{10}\rho = 11.62 + 1.5\log_{10}\left(\frac{T_\alpha}{10^9\ \mathrm{K}}\right) - 39.17\left(\frac{T_\alpha}{10^9\ \mathrm{K}}\right)^{-1} \tag{2.2.0.16}$$

Due to the accretion that persists during phase I of the explosion phase, the proto-NS continues to grow. The fraction of surface downflows roughly determines the fraction of shocked material that ends up in the proto-NS. Additionally, due to neutrino heating a fraction $\eta_{\rm acc}\eta_{\rm out}/|e_{\rm g}|$ of the accreted material is re-ejected. So, the baryonic mass of the NS as a function of $M_{\rm sh}$ is given by the differential equation

$$\frac{dM_{by}}{dM_{\rm sh}} = (1-\alpha_{\rm out})\left(1 - \frac{\eta_{\rm out}\eta_{\rm acc}}{|e_{\rm g}|}\right) \tag{2.2.0.17}$$

and evolution of explosion energy and the mass $M_{\rm sh}$ of the proto-NS during phase I of the explosion phase can thus be found using eqs. 2.2.0.3, 2.2.0.4, 2.2.0.11 and 2.2.0.17.

During phase II of the explosion phase, the bound material accumulated by the shock, the neutrino-driven wind (which helps in reducing the mass of the proto-NS) and the explosive burning in the shock affect the explosion energy. The works of [54, 55] justify the neglecting of the effect of the neutrino-driven wind on the final explosion and the properties of the remnant in this model and the consideration of only the other two contributions. Now, since all the matter that is swept by the shock contributes to the energy of the ejecta and not a fraction $\alpha_{\rm out}$, the diagnostic explosion energy growth can be defined in a similar way as in phase I as

$$\frac{dE_{diag}}{dM_{\rm sh}} = \epsilon_{\rm bind} + \epsilon_{\rm burn} \tag{2.2.0.18}$$

and the baryonic remnant mass $M_{\rm by}$ is left unchanged during this phase. By integrating eq. 2.2.0.18 up to the stellar surface we can find the final explosion energy $E_{\rm expl}$. Now, if $E_{\rm expl}$ is positive, we can find the gravitational mass of the NS, $M_{\rm NS}$, via the approximate formula given in [38, 39]

$$M_{\rm NS} = M_{\rm by} - 0.084\ M_\odot\left(\frac{M_{\rm NS}}{M_\odot}\right)^2 \tag{2.2.0.19}$$

However, if $E_{\rm diag}$ becomes negative at any $M_{\rm sh}$, if the remnant mass $M_{\rm NS}$ exceeds the maximum NS mass $M_{\rm max}$ or if the condition $\tau_{\rm adv}/\tau_{heat} = 1$ was never met during the whole pre- and explosion phases, then we set $E_{\rm expl} = 0$, assume that no explosion happens and that the entire start collapses into a BH, and the gravitational remnant mass M_{BH} is set to be equal to the pre-collapse mass of the star.

As a last note, let us state that during both phases I and II the mass of iron group elements that are produced by explosive nuclear burning $M_{\rm IG}$ is integrated by taking into account only a fraction $\alpha_{\rm out}$ will be ejected during phase I. This quantity, $M_{\rm IG}$, can be taken as a rough proxy for the nickel mass, but we have to be careful with this interpretation as ^{56}Ni is not the only iron group element that is produced by explosive nuclear burning when sufficiently high temperatures are reached. Additionally, the very crude "flashing" method we are employing based on estimated of the post-shock temperature cannot be expected to yield quantitatively reliable results. So, $M_{\rm IG}$ can at best be expected to agree with the actual nickel mass within a factor of ~ 2.

All of the parameters that have been introduced here have some typical value that is used in literature, however this value cannot represent the physical processes present in the star's evolution in some cases and they are of great importance since they could lead to the formation of compact objects either in the mass gap, or with an extreme mass ratio as in [28]. So, in the next chapter, we will discuss how we applied this model on some profiles for stars and the results that we got by performing a parameter study with this model.

Chapter 3

Simulations of Stellar Explosions

3.1 Simulations and Population Synthesis

As we said in the Introduction (Section 1), we are interested in studying the later stages (meaning the explosion phase and the aftermath) of the evolution of stars whose H-rich envelope has been removed (let us remind here that H stands for hydrogen and He for helium, and they will be used for simplicity). This process alters greatly the core structures of the star resulting in the formation of NSs and BHs with different masses compared to those formed by H-rich stars. Stars that have lost their H-rich envelope are called stripped-envelope stars, or He stars since their main element is now He.

To do this, we used published stellar profiles from [34, 35] of single non-rotating helium stars at 0.5, 0.75 and 1 times the solar metallicity $Z_{\odot}$. As input to the semi-analytic code of [27] (described in Section 2) we used the pre-SN stellar structures of the aforementioned profiles, in order to determine whether that star explodes into a SN or collapses into a BH. However, as we have said, the semi-analytic model depends on some parameters that are introduced in order to quantify some processes (for example the effects of turbulent phenomena on the shock radius, the conversion of neutrino heating into outflows, etc) shown in Table 3.1. These parameters are assigned some typical value in the literature, but this may be constricting the underlying physical processes that may occur during the final stages of stellar evolution. This can affect the outcome of the death of the star and also the properties of the remnant. In order to get a better understanding of stellar explosions and the remnants they leave behind, we will perform a parameter study where we will let each parameter take values in the range they are theorised to lie in.

We shall briefly review said parameters and state their purpose and their range of values in a table, so the reader can have a place to check quickly and not have to look through Section 2 to try and find the answer.

parameter	explanation	typical range
α_{out}	volume fraction of outflows	$0.3 \dots 0.7$
α_{turb}	shock expansion due to turbulent stresses	$1 \dots 1.4$
β	shock compression ratio during explosion phase	$3 \dots 7$
ζ	efficiency factor for conversion of accretion energy into ν luminosity	$0.5 \dots 1$
$\tau_{1.5}$	cooling timescale for 1.5 $M_{\odot}$ NS	$0.6s \dots 3s$
η_{out}	efficiency factor for conversion of neutrino heating to an outflow rate	$0 \dots 2$
M_{max}	maximum mass for a NS	$2M_{\odot} \dots 3M_{\odot}$

Table 3.1: Table of the model's parameters that were changed during simulations.

We created a parameter grid by first letting each parameter (excluding the metallicity for which we only consider the previous 3 values) take 3 values in the aforementioned interval which created 2187 combinations. The grid resolution (i.e. how many values each parameter takes) can be changed except for the metallicity which is fixed to these 3 values as they were used in creating the profiles with the MESA code.

In order to better understand the explosion mechanism, we need perform a population synthesis and study the remnants by means of their mass distribution. Its shape can reveal many insights of the explosion processes as shown in a similar study (they did only a population synthesis, not a parameter study) done in [56] where by using the same model and focusing only on the BHs, they found a bimodal BH mass distribution which is linked to the fact that carbon and neon burning becomes neutrino-dominated, altering the interior structures in such a way that is becomes difficult for the star to explode, thus leading to more BHs forming. In our case, we consider both NSs and BHs and we tread as follows.

First, we randomly sample the initial mass of a zero age main sequence (ZAMS) star using the Salpeter initial

mass function (IMF) [57]

$$p(M) \propto M^{-2.35} \tag{3.1.0.1}$$

This mass gets converted to a He core mass following the formula of [58]

$$M_{\text{He, ini}} \sim \begin{cases} 0.0385 M_{\text{ZAMS}}^{1.603}, & \text{if } M_{\text{ZAMS}} < 30 M_{\odot} \\ 0.5 M_{\text{ZAMS}} - 5.87 M_{\odot}, & \text{if } M_{\text{ZAMS}} \geq 30 M_{\odot} \end{cases} \tag{3.1.0.2}$$

Then, the resulting mass gets mapped into a mass for which we have a profile using a modified floor function, which returns the nearest integer or half-integer to the input mass as follows

$$M_{\text{for profile}} = \begin{cases} \lfloor M \rfloor, & \text{if } M \bmod int(M) < 0.5 \\ \lfloor M \rfloor + 0.5, & \text{if } M \bmod int(M) \geq 0.5 \end{cases} \tag{3.1.0.3}$$

where $\lfloor \cdot \rfloor$ is the floor function, which that takes as input a real number x, and gives as output the greatest integer less than or equal to x (meaning 3.9 gets rounded to 3) and in the code is is done using the $np.fix$ function of the NumPy [59] library, and int returns the integer part of the input and a mod b returns the remainder of the division a with b. This is the scheme we chose and it may not be realistic, but it enables us to correspond the He core mass to an already evolved stellar profile. From the data of the evolved profile, we got the final (gravitational) mass of the remnant. This process is repeated for 10000 samples for all combinations of parameters values. These resulting gravitational masses are recorded for further analysis.

3.2 Analysis for all 3 values of Z

From these data, we can find the mass gap (if present) in the remnant mass distribution. To do so, we extract the value of the M_{max} parameter that we have assigned in this case of our parameter study, and split further the data into NS masses and BH masses by checking whether the mass is lesser or equal to M_{max} (NS) or larger (BH). Then, we check if there are any data for NSs (as in some cases the values of the parameters it was made really hard for stars to explode and turn into a NS) and then we subtract the maximal value of the NS data from the minimal value of the BH data which gives us an estimation of the mass gap.

Out of the 6561 cases of the above population synthesis, which corresponds to 3 (from the values of Z) $\times$ 2187 (which are the total parameter values combinations), only 4566 (or $\sim 70\%$) exhibit a mass gap in the remnant mass (meaning NS + BH) distribution. This means that the rest 1995 (corresponding to $\sim 30\%$) of the cases do not exhibit a mass gap. Out of those, 1977 (or $\sim 99\%$) do so because these models predict no NSs, meaning that for these parameter values it is extremely hard for stars to explode. The rest 18 (or $\sim 1\%$) do not exhibit a mass gap because these models do not predict any BHs, which means that these parameter values make it so that stars explode really easily. Both of these cases are unnatural since we have observed both NSs and BHs in nature, and so they shall be labeled as unnatural and we remove them so as to not be taken into consideration in any further analysis.

For the rest of the analysis, we shall focus only on the BH data, as the data for NSs do not have the necessary resolution in order to be put through the following analysis as they suffer from numerical noice. For the BH mass distribution, we will analyse the shape and the structure of its distribution in order to gain information.

However, doing that graphically for all the parameter cases and values of Z will take ages, so in order to get information about the distribution shape in a programmingly way, we employ the method of Gaussian Mixture fitting. To each distribution we fit a Gaussian Mixture Model (GMM), which corresponds to the likelihood function, which for a datum x_i is given by

$$p(x_i|\vec{\theta}) = \sum_{i=1}^{N} \phi_i \mathcal{N}(\mu_i, \sigma_i) \tag{3.2.0.1}$$

where $\mathcal{N}(\mu, \sigma)$ is a normal (Gaussian) distribution with mean μ and variance σ^2, $\vec{\theta}$ is the parameter vector of the estimated μ_i, σ_i and ϕ_i values of the model, ϕ_i is the weight of the ith component with mean μ_i and standard deviation σ_i. For normalisation reasons, we have that $\sum_{i=1}^{N} \phi_i = 1$. In order to fit the GMM in our code, we used the $scikit-learn$ library [60]. More specifically, we used the $GaussianMixture$ model from the $mixture$ package. We iterated N with values from 1 to 10 and each instance corresponds to a different model that is fitted onto our data. In order to quantify the accuracy of the fit, we used the Bayesian Information Criterion (BIC) [61] which is formally defined as

$$BIC = k \ln(2) - 2 \ln\left(\hat{L}\right) \tag{3.2.0.2}$$

where k corresponds to the number of parameters that are estimated by the model M (each instance of the GMM in our case), n is the number of data points, and $\hat{L}$ is the maximized value of the likelihood function of the model M. The model's fit is more accurate the lower its BIC value is. Additionally, we split the data (the BH gravitational masses) into two subsets, $M_{\text{train}}^{\text{BH}}$ and $M_{\text{test}}^{\text{BH}}$ with a $75-25$ % split accordingly. We used the $M_{\text{train}}^{\text{BH}}$ to fit the model, and the $M_{\text{test}}^{\text{BH}}$ to find the BIC.

So, we created an array of models as mentioned above, which were trained using $M^{\rm BH}_{\rm train}$ and their BIC score was evaluated using $M^{\rm BH}_{\rm test}$. Then, we found the minimum value of the BIC array and the corresponding model, which shall be called the best model (BM) hereafter. We also saved the number of components $N_{\rm comp}$ of the BM. Since the maximum value of N is set to 10, we consider any distribution that had $N_{\rm comp} > 6$ as one having a complex structure that cannot be described adequately by discrete Gaussian processes. Then, we used the criteria described in [62] to get information abut the structure of the distributions, and more specifically the statistic

$$D = 2^{1/2} \frac{|\mu_j - \mu_{j+1}|}{\sqrt{\sigma_j^2 + \sigma_{j+1}^2}} \tag{3.2.0.3}$$

which gauges the separation between two Gaussians, $\mathcal{N}(\mu_j, \sigma_j)$ and $\mathcal{N}(\mu_{j+1}, \sigma_{j+1})$, in order to find any information about multimodality in the distributions. For a clean separation we expect $D > 2$, as stated in [62]. We have used the j and $j+1$ indices here as we have multiple components in our models, and we want to check the distance between any two consecutive components. Additionally, we search for components that have a distance $D > 4$, which we consider that they comprise distinct groups, and components that have a distance $D > 8$ as these have a large separation.

As stated before, 18 cases did not produce any BHs and 1977 cases did not predict NSs, which means that only 4566 cases have a (physically acceptable) BH mass distribution. Now, out of those 4566 cases, 2323 (or $\sim 51\%$) have more than 6 components in their BM, as seen in Figure 3.1, which corresponds in a complex structure that cannot be adequately described by discrete Gaussian processes.

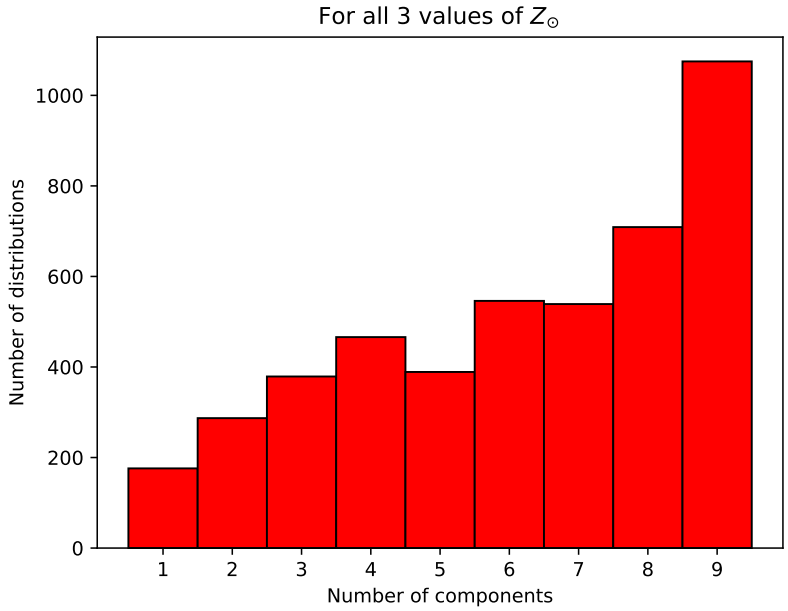

Figure 3.1: Histogram of the number of components of the best GMM fitted to the BH mass distribution in each case for all values of Z.

Furthermore, 2702 (or $\sim 59\%$) cases have more than 1 distinct groups, as seen in Figure 3.2a, with of them 1486 (or $\sim 55\%$) having at least one set of consecutive groups with a large gap between them, Figure 3.2b. A large number of distinct groups indicates a sporadic spread in the BH mass distribution, meaning that the models can only predict the corresponding BH masses, leaving a lot of gaps in the process. This is accompanied by the fact that there exist models with many large gaps between their distinct groups. This leaves certain BH masses out of the equation.

These results are, however, cumulative in terms of metallicity, which leads to the overshadowing of the effect of the metallicity in the mass gap and the BH mass distribution. Let us now study each metallicity case separately and see what information we get, considering that metallicity affects the evolution of a star as stated in [63] and in the references therein. Additionally, for each Z value, we will plot the remnant mass (given by the gravitational mass $M_{\rm grav}$) as a function of final mass of the star pre-collapse ($M_{\rm final}$), as well as we will present to random cases in order to paint a picture for the process. Let us start with the lowest metallicity, $Z = 0.5\ Z_\odot$.

3.2.1 For $Z = 0.5\ Z_\odot$

Limiting the data to those for $Z = 0.5\ Z_\odot$, we get 2187 total cases, which is exactly the number we expected given the number of combinations of values for the parameters we stated in Section 3.1. Out of those, 1557 (or $\sim 71\%$) have a mass gap, with the remaining 630 (or $\sim 29\%$) not having a mass gap due to not predicting any NSs. These

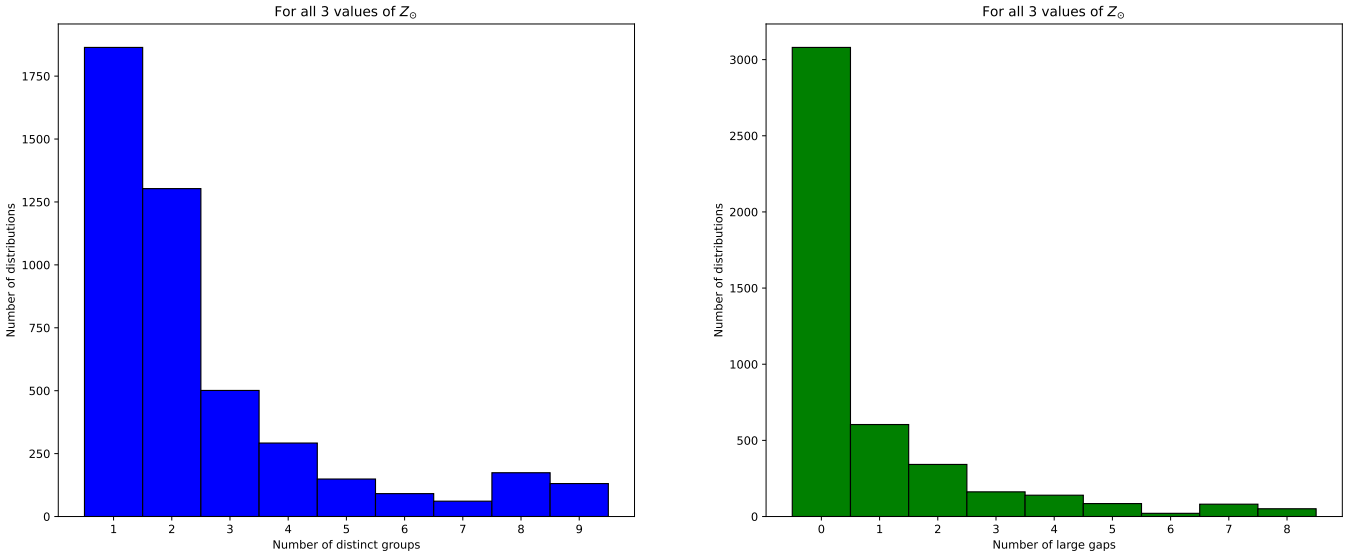

(a) (b)

Figure 3.2: Histograms of two different structural characteristics derived from the statistic 3.2.0.3 of the BH mass distribution for all values of Z. Specifically, 3.2a depicts the number of distinct groups, meaning $D > 4$, found in the distributions. 3.2b depicts the number of large groups, meaning $D > 8$, encountered in the distributions.

630 cases are labeled unphysical and are removed from the rest of the analysis. Moving our attention to the BH mass distribution for $Z = 0.5\ Z_\odot$, we get 1557 cases, since we have removed the unphysical ones. Out of the remaining, 738 (or $\sim 47\%$) have more than 6 components in their BM, as seen in Figure 3.3. Additionally, 757 (or $\sim 49\%$) have at least 2 distinct groups, see Figure 3.4a, and out of those 363 (or $\sim 48\%$) have at least one set of consecutive groups with a large gap between them, as seen in Figure 3.4b.

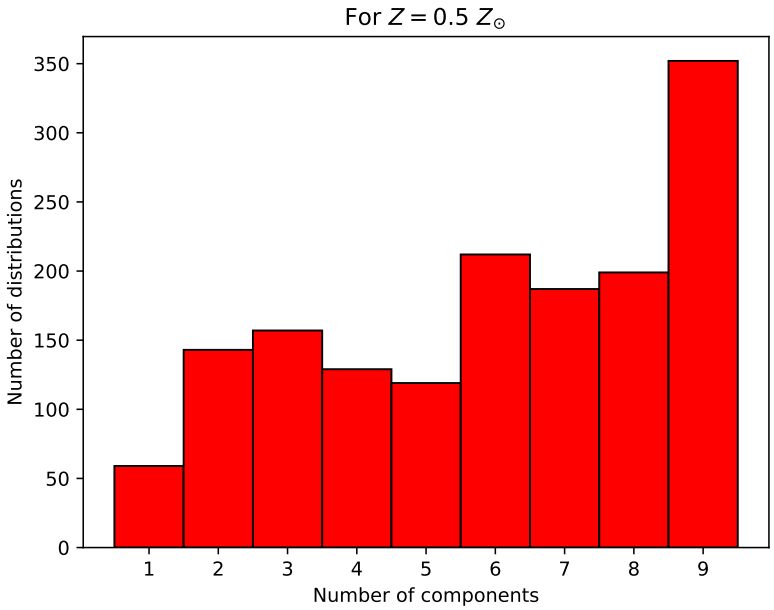

Figure 3.3: Histogram of the number of components of the best GMM fitted to the BH mass distribution in each case for $Z = 0.5\ Z_\odot$.

Let us take a better look at two cases. These were chosen randomly among the numerous others as to eliminate bias to show the good cases. The only condition we imposed it that it corresponds to a physically acceptable case of parameter values, as we have argued above. The first of these two cases has the parameter values shown in Table 3.2. We plotted the remnant mass distribution, together with the best GMM fit, and the BH mass distribution, also with its best GMM fit, for this case, and are shown in Figure 3.5a and Figure 3.5b respectively.

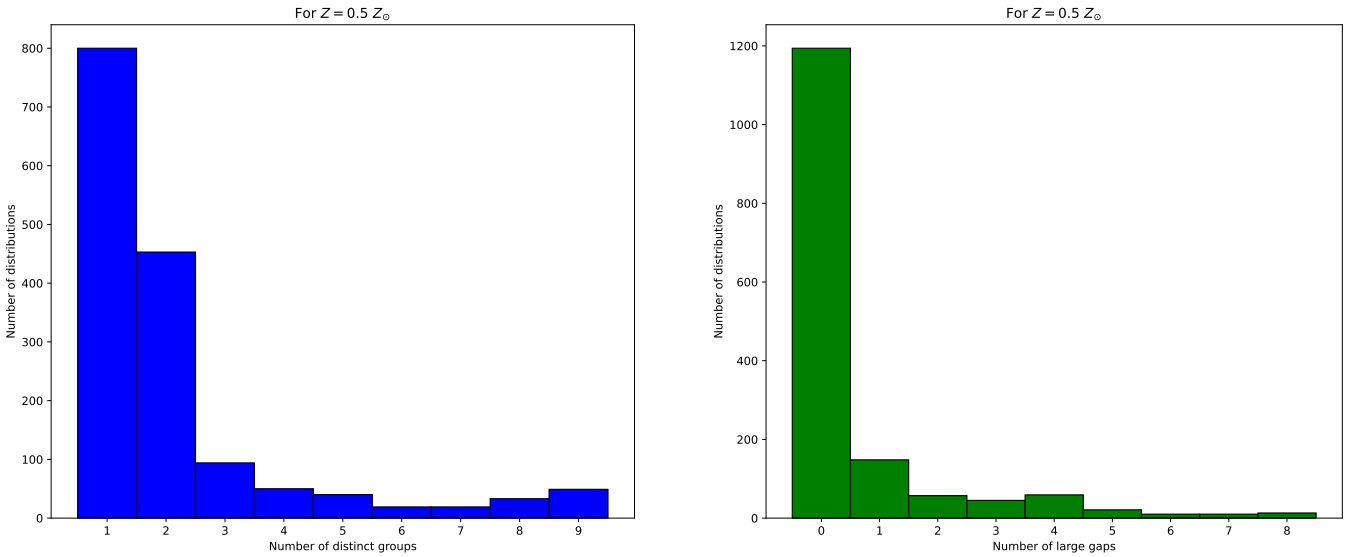

(a) (b)

Figure 3.4: Histograms of two different structural characteristics derived from the statistic 3.2.0.3 of the BH mass distribution for $Z = 0.5\ Z_\odot$. Specifically, a depicts the number of distinct groups, meaning $D > 4$, found in the distributions. b depicts the number of large groups, meaning $D > 8$, encountered in the distributions.

Parameter Values						
β	α_{out}	η_{out}	ζ	α_{turb}	$\tau_{1.5}$	M_{max}
5.0	0.3	2.0	0.5	1.2	3.0	2.5

Table 3.2: Parameter values for the first example for $Z = 0.5$.

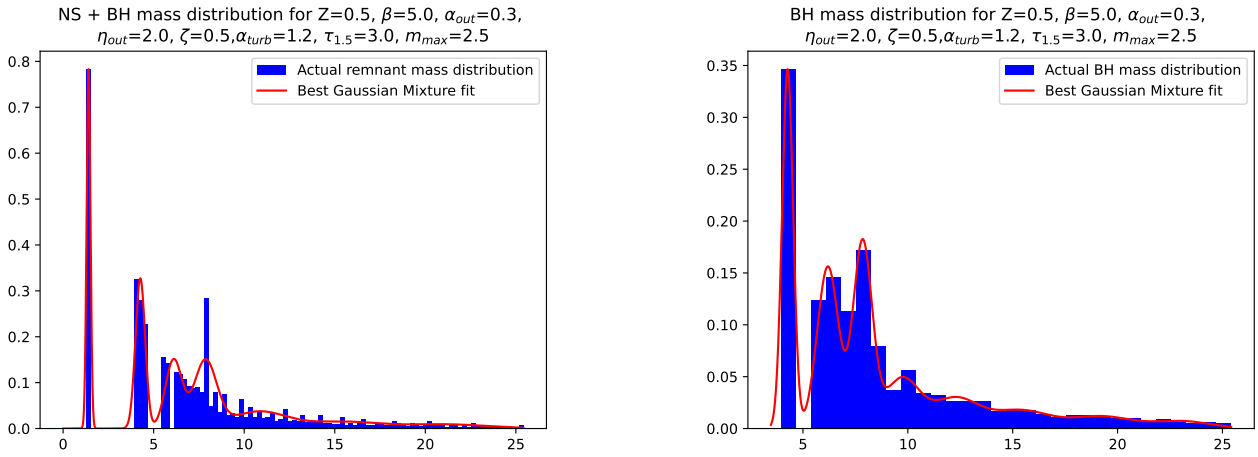

(a) (b)

Figure 3.5: Remnant mass distribution a along with the best GMM fit (red line) and BH mass distribution b and along with the best GMM fit for $Z = 0.5$, $\beta = 5.0$, $\alpha_{\text{out}} = 0.3$, $\eta_{\text{out}} = 2.0$, $\zeta = 0.5$, $\alpha_{\text{turb}} = 1.2$, $\tau_{1.5} = 3.0$, $M_{\text{max}} = 2.5$.

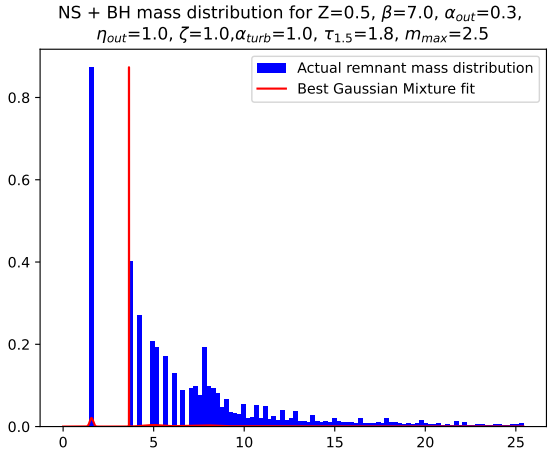

(a)

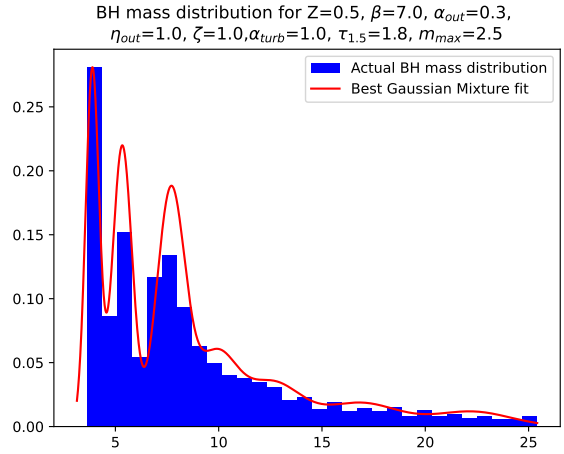

(b)

Figure 3.6: Remnant mass distribution a along with the best GMM fit (red line) and BH mass distribution b and along with the best GMM fit for $Z = 0.5$, $\beta = 7.0$, $\alpha_{\rm out} = 0.3$, $\eta_{\rm out} = 1.0$, $\zeta = 1.0$, $\alpha_{\rm turb} = 1.0$, $\tau_{1.5} = 1.8$, $M_{\rm max} = 2.5$.

We can see that the remnant mass distribution in Figure 3.5a has some structures, but the most important for our analysis is there is a mass gap of 2.4 $M_\odot$. This is a prime example of a problematic NS distribution, since it predicts only one mass for NSs. Furthermore, The BH mass distribution in Figure 3.5b is bimodal (has 2 distinct groups) with no large gaps between the groups and its best GMM fit has 8 components (as can be seen by carefully counting the number of Gaussian peaks).

The second case has the parameter values shown in Table 3.3. We can see that the remnant mass distribution in this case shown in Figure 3.6a has a mass gap of 2.0 $M_\odot$, which is the characteristic we are looking for. The BH mass distribution of this case, shown in Figure 3.6b, is not bimodal but nevertheless has 2 distinct groups, and as it can be seen the best fit has 8 components.

Parameter Values						
β	$\alpha_{\rm out}$	$\eta_{\rm out}$	ζ	$\alpha_{\rm turb}$	$\tau_{1.5}$	$M_{\rm max}$
7.0	0.3	1.0	1.0	1.0	1.8	2.5

Table 3.3: Parameter values for the second example for $Z = 0.5$.

Finally, let us take a look at the remnant mass $M_{\rm grav}$ - final mass $M_{\rm final}$ plot, Figure 3.7. We can clearly see there that there is a clear correlation between $M_{\rm final}$ and the mass of a BH M_{BH}, whereas for NSs is not evident. This is probably due to the short range of NS mass values as opposed to the BHs, but a similar tendency as in the BHs can be observed for the NSs as well. We expect the final mass to affect the remnant mass, and any results that point to the other direction shall be attributed to an unphysical case. Let us move now to the $Z = 0.75\ Z_\odot$ case.

3.2.2 For $Z = 0.75\ Z_\odot$

Focusing now on the data for $Z = 0.75\ Z_\odot$, we again get 2187 total cases. Out of those, 1605 (or $\sim 73\%$) have a mass gap in their remnant mass distribution, whereas the remaining 582 (or $\sim 27\%$) do not with all of them not predicting any NSs, thus we labeled them unphysical and removed them from the rest of the analysis. For the remaining 1605, 917 (or $\sim 57\%$) have more than 6 components in their BM, as seen in Figure 3.8, and 1028 (or $\sim 64\%$) have at least two distinct groups, Figure 3.9a, with 556 (or $\sim 55\%$) of them having at least a set of two consecutive groups that have a large gap between them, Figure 3.9b.

Let us now proceed to the two examples for this case. The first example has the parameter values shown in Table 3.4

Parameter Values						
β	$\alpha_{\rm out}$	$\eta_{\rm out}$	ζ	$\alpha_{\rm turb}$	$\tau_{1.5}$	$M_{\rm max}$
7.0	0.5	1.0	0.75	1.0	0.6	2.0

Table 3.4: Parameter values for the first example for $Z = 0.75$.

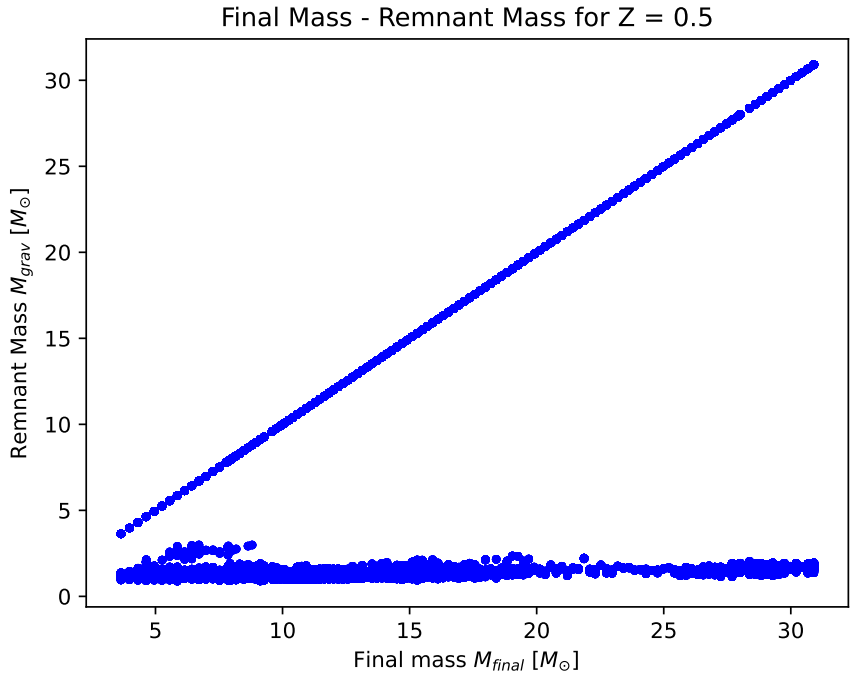

Figure 3.7: Remnant mass $M_{\rm grav}$ - Final mass $M_{\rm final}$ plot for $Z = 0.5$.

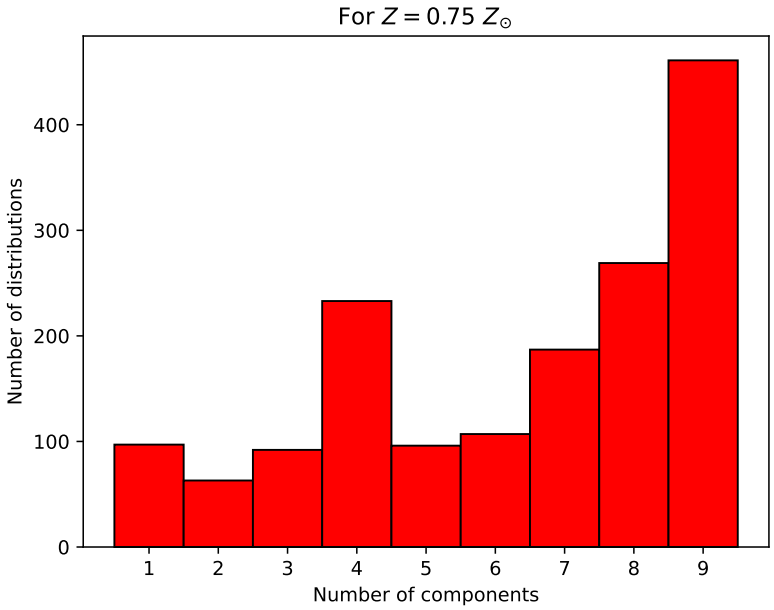

Figure 3.8: Histogram of the number of components of the best GMM fitted to the BH mass distribution in each case for $Z = 0.75\ Z_\odot$.

We then plot the remnant mass distribution, Figure 3.10a, which has a mass gap of 1.9 $M_\odot$, which is the characteristic we are looking for. The remnant mass distribution as it can be seen has a weird structure. This peculiarity may be an artifact of the binning of the histogram. The BH mass distribution of this case, shown in Figure 3.10b, is quadramodal which may or may not be a result of the binning. The aforementioned analysis said that it has 6 distinct groups and 3 large gaps. The large gaps can be easily seen, but one can only distinguish 4 groups (5 if you consider that the two peaks in the second mode are sufficiently apart and 6 if one used the same argument for the fourth mode). Additionally, the best GMM fit has 7 components, which is hard to see in the plot. Let us note here that in all the plots where also the best GMM fit is shown, we have fixed the scale of the best fit by multiplying it with the ratio max(BH distribution)/max(best GMM fit), resulting in a scaled down version.

For the second example, we have the parameter values shown in Table 3.5. The plot for the remnant mass distribution is shown in Figure 3.11a. This is also an example why the NS mass distribution is problematic. It

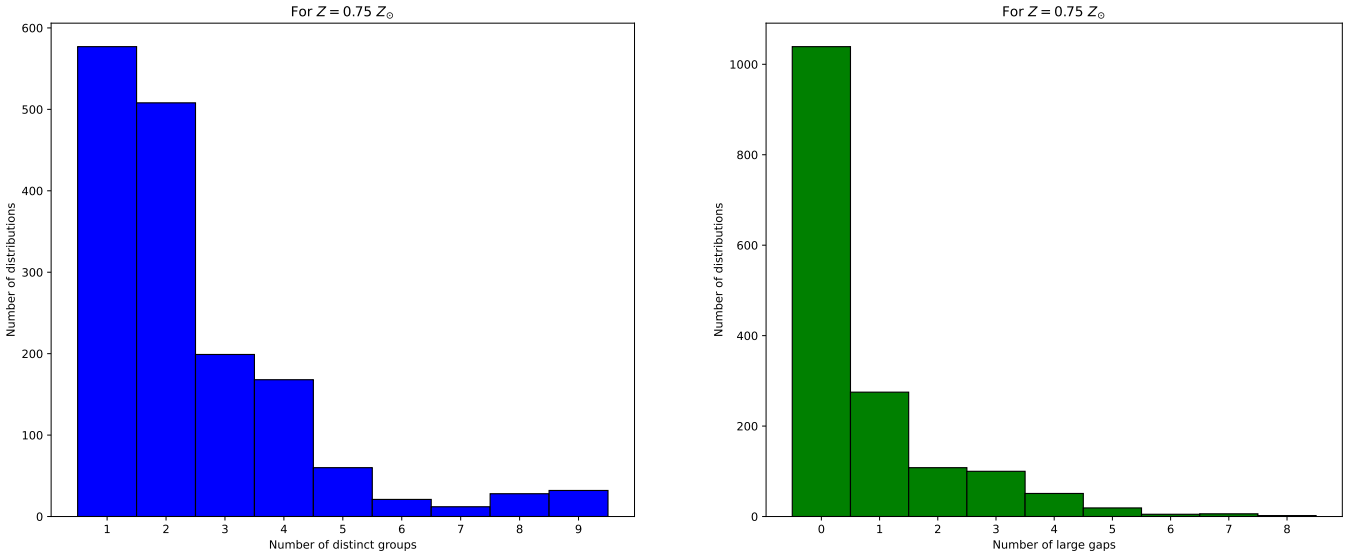

(a) (b)

Figure 3.9: Histograms of two different structural characteristics derived from the statistic 3.2.0.3 of the BH mass distribution for $Z = 0.75\ Z_\odot$. Specifically, a depicts the number of distinct groups, meaning $D > 4$, found in the distributions. b depicts the number of large groups, meaning $D > 8$, encountered in the distributions.

overshadows the BH mass distribution and causes the fitting process to derail. Nevertheless, the distribution has a mass gap of 18.6 $M_\odot$, but unfortunately it cannot be seen in the plot. Turning our attention to the BH mass distribution in Figure 3.11b, we can clearly see that here also the fit, which has 9 components, is not that accurate, despite it being the best one. Our analysis process said that the distribution has 6 distinct groups, but they are not easily seen in the plot, with 4 large gaps, which can be discerned. The inbetween not-large gaps that give the distribution a weird structure are most probably a result of the binning of the data.

Parameter Values						
β	α_{out}	η_{out}	ζ	α_{turb}	$\tau_{1.5}$	M_{max}
3.0	0.3	1.0	0.5	1.4	0.6	2.0

Table 3.5: Parameter values for the second example for $Z = 0.75$.

Unfortunately, due to some complications that have yet to be resolved in the process of making the $M_{\text{final}} - M_{\text{grav}}$ plot, it will not be displayed here. Once they are resolved, it will be added. Finally, let us focus on $Z = 1.0\ Z_\odot$.

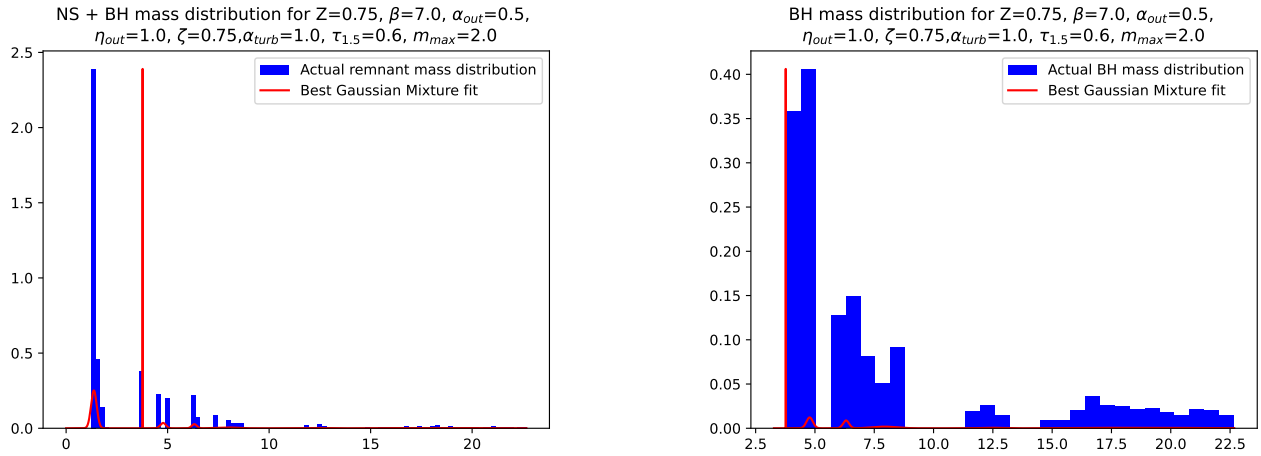

(a) (b)

Figure 3.10: Remnant mass distribution a along with the best GMM fit (red line) and BH mass distribution b and along with the best GMM fit for $Z = 0.75$, $\beta = 7.0$, $\alpha_{\text{out}} = 0.5$, $\eta_{\text{out}} = 1.0$, $\zeta = 0.75$, $\alpha_{\text{turb}} = 1.0$, $\tau_{1.5} = 0.6$, $M_{\text{max}} = 2.0$.

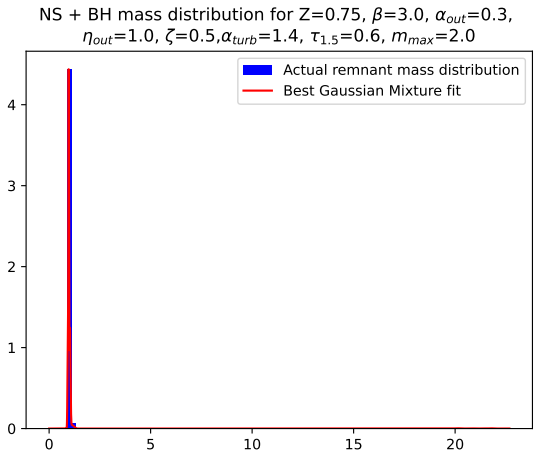

(a)

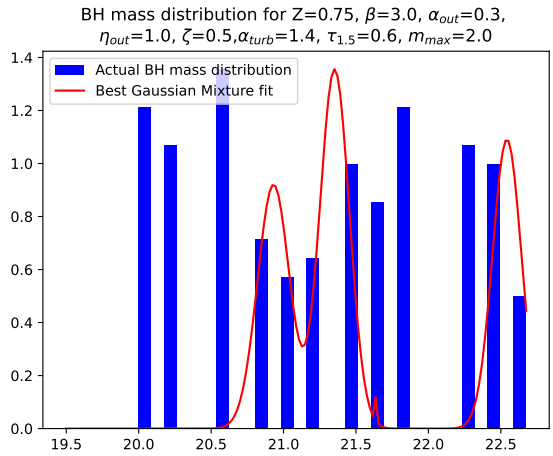

(b)

Figure 3.11: Remnant mass distribution a along with the best GMM fit (red line) and BH mass distribution b and along with the best GMM fit for $Z = 0.75$, $\beta = 3.0$, $\alpha_{\rm out} = 0.3$, $\eta_{\rm out} = 1.0$, $\zeta = 0.5$, $\alpha_{\rm turb} = 1.4$, $\tau_{1.5} = 0.6$, $M_{\rm max} = 2.0$.

3.2.3 For $Z = 1.0\ Z_\odot$

For $Z = 1.0\ Z_\odot$ we have a total of 2169 cases, due to the 18 that did not predict any BHs that where removed in Section 3.2. Out of those, 1404 (or $\sim 65\%$) have a mass gap, while the rest 765 (or $\sim 35\%$) do not have one as they do not predict any NSs, and as before they are removed. The BH mass distributions of the remaining 1404 cases where fitted with GMMs, of which the BM of 668 (or $\sim 48\%$) has more than 6 components, as seen in Figure 3.12. 917 (or $\sim 65\%$) of the distributions have at least two distinct groups, as seen in Figure 3.13a, and 557 (or $\sim 61\%$) of them have at least a set of consecutive groups that have a large gap inbetween them, see Figure 3.13b.

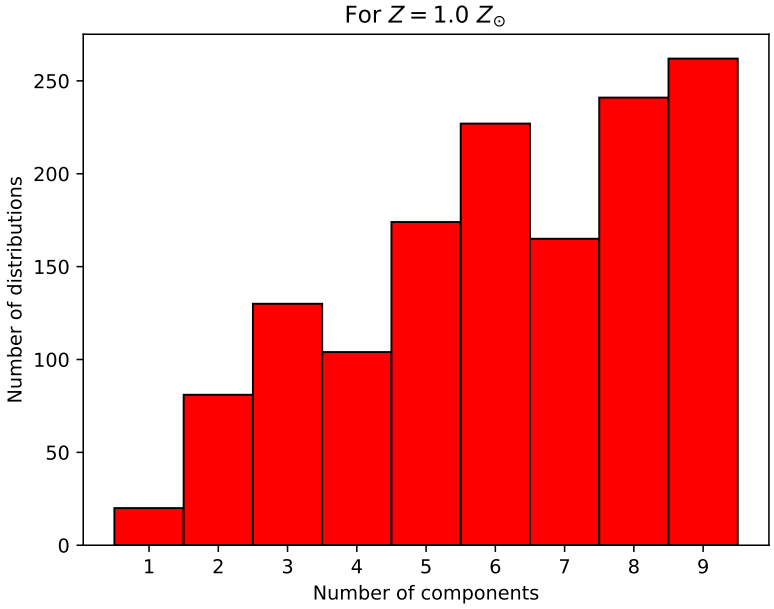

Figure 3.12: Histogram of the number of components of the best GMM fitted to the BH mass distribution in each case for $Z = 1.0\ Z_\odot$.

Let us take a look at the two examples for this case as well. The first example has the parameter values shown in Table 3.6. The plot for the remnant mass distribution is shown in Figure 3.14a. In the plot we can see that the number of NSs that this model predicted are few and peculiarly distributed, and we can see some gaps in the distribution, but these may or may not exist as in Figure 3.14b they are not there. Nevertheless, since we have NSs, we can define a mass gap, which in this case is 1.7 $M_\odot$. The BH mass distribution is shown in Figure 3.14b. First thing we can see, is that due to the low number of NSs and their peculiar distribution, both the remnant and the BH mass distributions have the same best model fit. It has 7 components (some of them are hard to discern) and the analysis identified only one distinct group, which means that the gaps in Figure 3.14a are probably an artifact of the binning. Since the

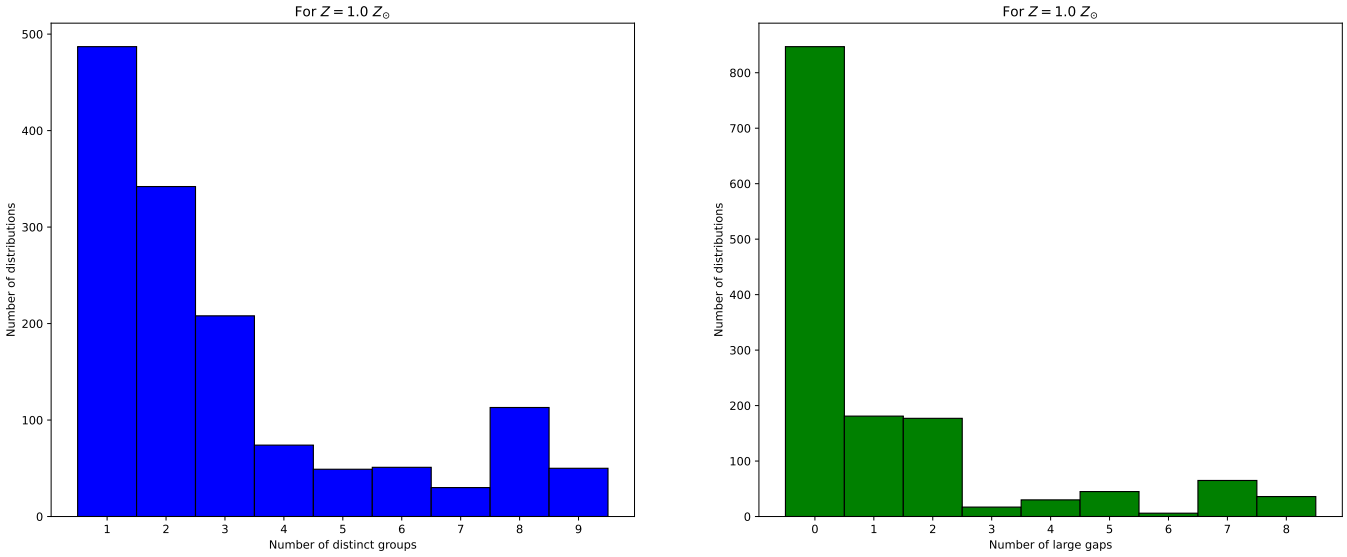

(a) (b)

Figure 3.13: Histograms of two different structural characteristics derived from the statistic 3.2.0.3 of the BH mass distribution for $Z = 1.0\ Z_\odot$. Specifically, a depicts the number of distinct groups, meaning $D > 4$, found in the distributions. b depicts the number of large groups, meaning $D > 8$, encountered in the distributions.

distribution has only 1 distinct group, we cannot define a large gap.

For the second example, the parameters have the values shown in Table 3.7. This case is an example of the peculiar cases that were encountered in the population synthesis seeded from the parameter study. First of all, it is another case of a problematic NS distribution as we can see from the remnant mass distribution in Figure 3.15a. The NS distribution overshadows the one for the BHs, but due to the presence of both remnant types we can define a mass gap, and it is 1.8 $M_\odot$. Also, we can see a gap in the BH mass distribution that is not present or detected in the fitting done in Figure 3.15b. Furthermore, the best fit in Figure 3.15b, that has 6 components, identifies 6 distinct groups, all of which have a large gap inbetween them. However, the distribution does not show anything like this. From the BH mass distribution, one can clearly see 3 distinct groups (the third one being on the far right side and it is barely visible), with 2 large gaps. This indicates that the best fitted model is wrong, or that the binning of the data does not allow these structures to reveal themselves. It is not clear which is the case here. Similar cases were most probably present throughout the study and if we want to eliminate them, then we must find a systematic way to do so.

In addition, let us look at the $M_{\rm final} - M_{\rm grav}$ plot for this case of metallicity, which is shown in Figure 3.16. Here, as well as in the $Z = 0.5\ Z_\odot$ case shown in Figure 3.7, we can see a clear correlation of $M_{\rm grav}$ with $M_{\rm final}$ whereas it is not apparent for the NSs, due to the different range of values, but a similar tendency as in the BHs can be observed for the NSs as well.

Parameter Values						
β	$\alpha_{\rm out}$	$\eta_{\rm out}$	ζ	$\alpha_{\rm turb}$	$\tau_{1.5}$	$M_{\rm max}$
7.0	0.3	0.0	1.0	1.4	0.6	3.0

Table 3.6: Parameter values for the first example for $Z = 1.0$.

Parameter Values						
β	$\alpha_{\rm out}$	$\eta_{\rm out}$	ζ	$\alpha_{\rm turb}$	$\tau_{1.5}$	$M_{\rm max}$
7.0	0.3	1.0	0.5	1.4	0.6	2.0

Table 3.7: Parameter values for the second example for $Z = 1.0$.

Looking at Figures 3.3, 3.8 and 3.12 and the statistics describing them, we can see that almost $\sim 50\%$ of the distributions in each case have a complex structure that is difficult to describe by means of discrete Gaussian processes. Additionally, the number of models with numerous (lets say more than 3) sets of consecutive groups that have a large gap between them as can be seen from Figures 3.4b, 3.9b and 3.13b is steadily low, since many large gaps hint of a disjoint and sporadic distribution which cannot predict some BH masses, and that may be a problem since in the realm of stellar BHs the mass spectrum is expected to be somewhat coherent. Finally, from all 3 sets of Figures 3.4a & b, 3.9a & b and 3.13a & b we can see that the number of distributions with a single distinct group or the number of

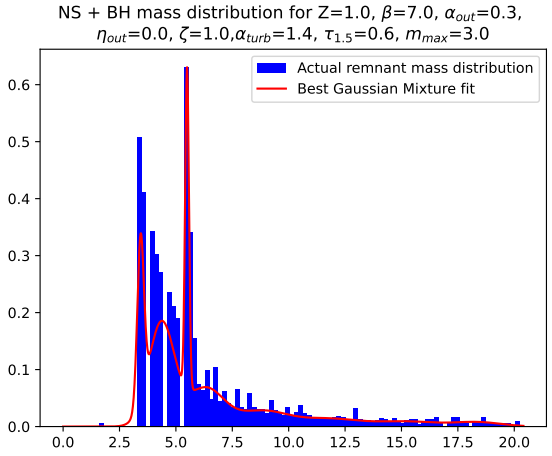

(a)

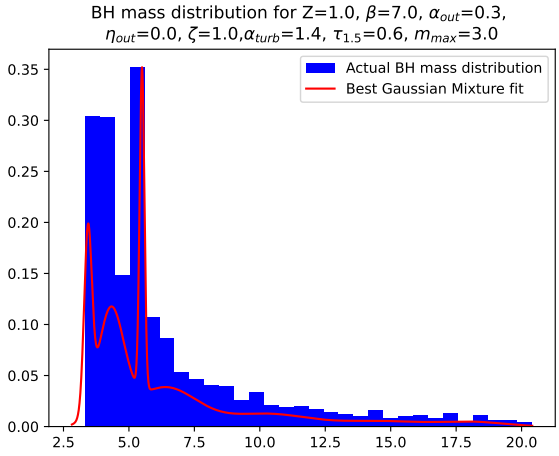

(b)

Figure 3.14: Remnant mass distribution a along with the best GMM fit (red line) and BH mass distribution b and along with the best GMM fit for $Z = 1.0$, $\beta = 7.0$, $\alpha_{\text{out}} = 0.3$, $\eta_{\text{out}} = 0.0$, $\zeta = 1.0$, $\alpha_{\text{turb}} = 1.4$, $\tau_{1.5} = 0.6$, $M_{\text{max}} = 3.0$.

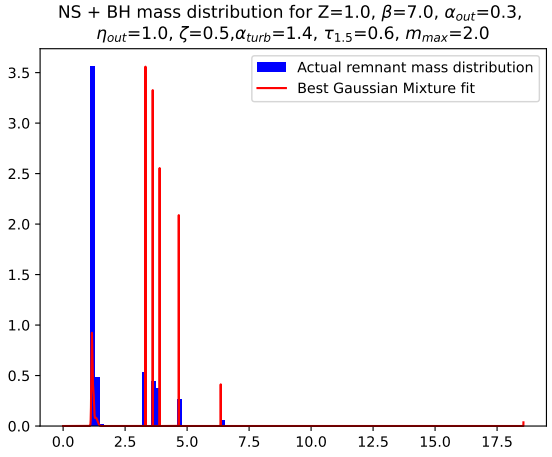

(a)

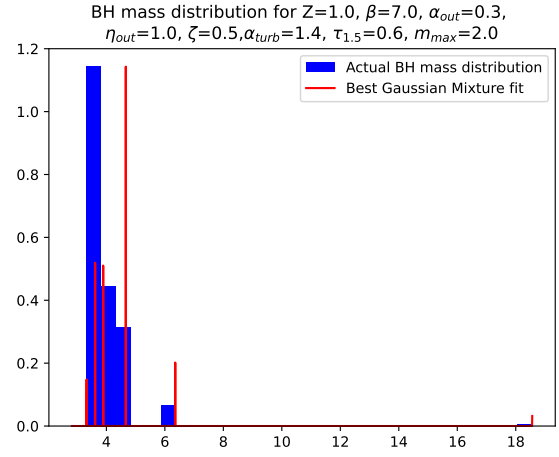

(b)

Figure 3.15: Remnant mass distribution a along with the best GMM fit (red line) and BH mass distribution b and along with the best GMM fit for $Z = 1.0$, $\beta = 7.0$, $\alpha_{\text{out}} = 0.3$, $\eta_{\text{out}} = 1.0$, $\zeta = 0.5$, $\alpha_{\text{turb}} = 1.4$, $\tau_{1.5} = 0.6$, $M_{\text{max}} = 2.0$.

distributions without any large gaps in them is decreasing as Z increases. This indicates the arising of more structures in the distributions.

Finally, let us remark here that this work in not complete yet. The model of [27] is outdated and as such is missing the effects of fallback on the newly formed compact object. In [64], which is an updated version of [27], the shock can continue to spread outward, even when the NS has reached its maximum mass limit because of ongoing material accumulation following an explosion. This shock keeps developing until it either surpasses the velocity required to escape, stopping the material from falling onto the remaining object, or weakens to become a faint sound pulse, ejecting a small portion of the surrounding envelope. We expect this to affect the outcome of the SN. Additionally, we want to extend our parameter and population synthesis across cosmic time, as explained in the subsection 6.5.2 in [65], to better understand the relation between SN explosion physics and redshift z. This will also probe the BH mass distribution across z.

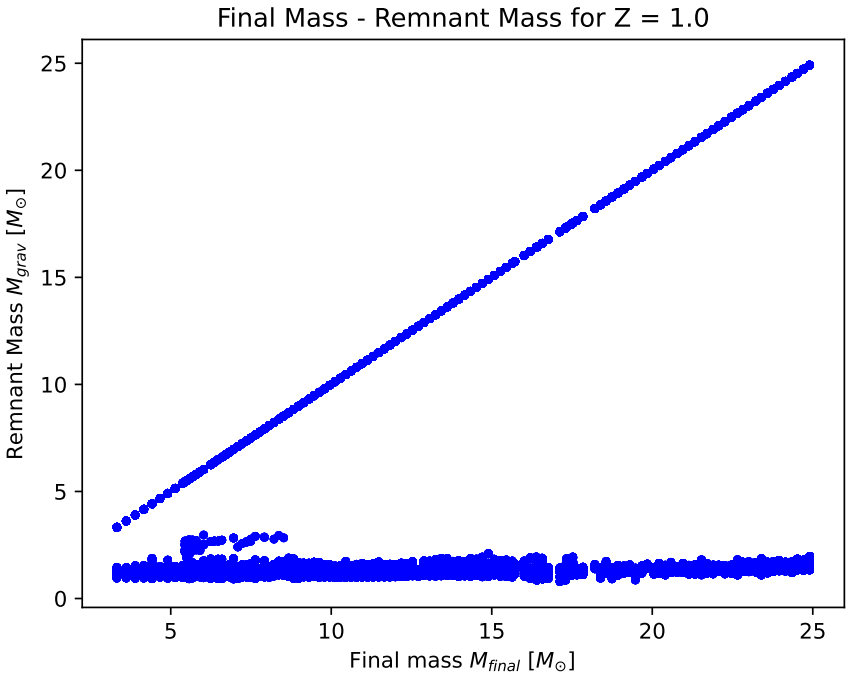

Figure 3.16: Remnant mass M_{grav} - Final mass M_{final} plot for $Z = 1.0$.

Chapter 4

Conclusions

In the preceeding chapters we described the model [27] we used, the parameters whose values we are interested in investigating further, Table 3.1, and the population synthesis we performed using published non-rotating binary-stripped star profiles for 3 values of metallicity $Z = 0.5, 0.75, 1.0\ Z_{\odot}$, in order to gauge the remnant (NS + BH), NS and BH mass distributions, and the process which we created in order to study these distributions (although the lack of resolution in the NS case lead us into to not taking this distribution into account when performing this analysis). Out of said analysis, it was found that $\sim 30\%$ combinations of parameter values were labeled unphysical as they failed to predict any NSs or BHs with the model [27]. Of the remaining physically acceptable cases, it was found that $\sim 51\%$ of them exhibited a complex structure via means of GMM fitting. Furthermore, $\sim 59\%$ of the physically acceptable cases had more than one distinct group in their distribution, with $\sim 55\%$ of those having at least one large gap inbetween two consecutive groups. This information hints on multimodal structures in these distributions.

Next, we repeated this analysis for each value of the metallicity in order to probe the effect of the metallicity in the evolution and the structures of the distributions. This analysis showed that Z affects the structures found in the BH mass distributions, which is expected, also the number of models with complex structured distributions varies between the Z values, but further simulations should be done in order to answer that definitely. In addition, we saw 2 examples in each case and elaborated on the problematic nature of the NSs distribution and the accuracy of the fitted GMM in cases of distributions with weird structures. Lastly, we plotted the remnant mass as a function of the final mass in order to elucidate the relation between these two masses.

Lastly, this work is still in progress, as we intend on using the updated version of [27], [64], which takes into account the effect of fallback onto the newly formed compact object, and also to extend this study across cosmic time following the prescription in Section 6.5.2 of [65] in order to gauge the effects of the redshift z in all of this.

Chapter 5

Acknowledgments

This line of work would not be possible without the contribution of some important people. First, I would like to thank Dr John Antoniadis for his mentorship during the development of this Master's thesis, as without his help this would not have been possible. In addition, I would like to thank my family for their support throughout my studies, my girlfriend and friends for their support (emotional and not), especially during the difficult times while debugging the code which proved detrimental at times. This work is done and funded under the project European Pulsar Interior Composition Survey (EPICS).

Chapter 6

Bibliography

[1] Y Gotberg, S E de Mink, M McQuinn, E Zapartas, J H Groh, and C Norman. Contribution from stars stripped in binaries to cosmic reionization of hydrogen and helium. *Astron. Astrophys.*, 634:A134, 2020.

[2] C. J. Evans, W. D. Taylor, V. Hénault-Brunet, H. Sana, A. de Koter, S. Simón-Díaz, G. Carraro, T. Bagnoli, N. Bastian, J. M. Bestenlehner, A. Z. Bonanos, E. Bressert, I. Brott, M. A. Campbell, M. Cantiello, J. S. Clark, E. Costa, P. A. Crowther, S. E. de Mink, E. Doran, P. L. Dufton, P. R. Dunstall, K. Friedrich, M. Garcia, M. Gieles, G. Gräfener, A. Herrero, I. D. Howarth, R. G. Izzard, N. Langer, D. J. Lennon, J. Maíz Apellániz, N. Markova, F. Najarro, J. Puls, O. H. Ramirez, C. Sabín-Sanjulián, S. J. Smartt, V. E. Stroud, J. Th. van Loon, J. S. Vink, and N. R. Walborn. The VLT-FLAMES Tarantula Survey. I. Introduction and observational overview. *Astronomy & Astrophysics*, 530:A108, June 2011.

[3] J. Maíz Apellániz, R. H. Barbá, M. Pantaleoni González, M. Weiler, B. C. Reed, R. Fernández Aranda, P. Crespo Bellido, A. Sota, E. J. Alfaro, and J. A. Molina Lera. The gaia view on massive stars: Edr3 and what to expect from dr3, 2022.

[4] Maryam Modjaz, Claudia P. Gutiérrez, and Iair Arcavi. New regimes in the observation of core-collapse supernovae. *Nature Astronomy*, 3:717–724, August 2019.

[5] Alejandro Vigna-Gómez, Coenraad J Neijssel, Simon Stevenson, Jim W Barrett, Krzysztof Belczynski, Stephen Justham, Selma E de Mink, Bernhard Müller, Philipp Podsiadlowski, Mathieu Renzo, Dorottya Szécsi, and Ilya Mandel. On the formation history of Galactic double neutron stars. *Monthly Notices of the Royal Astronomical Society*, 481(3):4009–4029, 09 2018.

[6] N. Langer. Presupernova Evolution of Massive Single and Binary Stars. *Annual Review of Astronomy & Astrophysics*, 50:107–164, September 2012.

[7] Hugues Sana and Christopher J. Evans. The multiplicity of massive stars. In Coralie Neiner, Gregg Wade, Georges Meynet, and Geraldine Peters, editors, *Active OB Stars: Structure, Evolution, Mass Loss, and Critical Limits*, volume 272, pages 474–485, July 2011.

[8] H. Sana, S. E. de Mink, A. de Koter, N. Langer, C. J. Evans, M. Gieles, E. Gosset, R. G. Izzard, J. B. Le Bouquin, and F. R. N. Schneider. Binary Interaction Dominates the Evolution of Massive Stars. *Science*, 337(6093):444, July 2012.

[9] H. Sana, J.-B. Le Bouquin, S. Lacour, J.-P. Berger, G. Duvert, L. Gauchet, B. Norris, J. Olofsson, D. Pickel, G. Zins, O. Absil, A. de Koter, K. Kratter, O. Schnurr, and H. Zinnecker. Southern massive stars at high angular resolution: Observational campaign and companion detection. *The Astrophysical Journal Supplement Series*, 215(1):15, nov 2014.

[10] Maxwell Moe and Rosanne Di Stefano. Mind Your Ps and Qs: The Interrelation between Period (P) and Mass-ratio (Q) Distributions of Binary Stars. *The Astrophysical Journal Supplement Series*, 230(2):15, June 2017.

[11] Ph. Podsiadlowski, P. C. Joss, and J. J. L. Hsu. Presupernova Evolution in Massive Interacting Binaries. *The Astrophysical Journal*, 391:246, May 1992.

[12] S. C. Yoon, S. E. Woosley, and N. Langer. Type Ib/c Supernovae in Binary Systems. I. Evolution and Properties of the Progenitor Stars. *The Astrophysical Journal*, 725(1):940–954, December 2010.

[13] Shenar, T., Gilkis, A., Vink, J. S., Sana, H., and Sander, A. A. C. Why binary interaction does not necessarily dominate the formation of wolf-rayet stars at low metallicity. *Astronomy & Astrophysics*, 634:A79, 2020.

[14] Langer, N., Schürmann, C., Stoll, K., Marchant, P., Lennon, D. J., Mahy, L., de Mink, S. E., Quast, M., Riedel, W., Sana, H., Schneider, P., Schootemeijer, A., Wang, C., Almeida, L. A., Bestenlehner, J. M., Bodensteiner, J., Castro, N., Clark, S., Crowther, P. A., Dufton, P., Evans, C. J., Fossati, L., Gräfener, G., Grassitelli, L., Grin, N., Hastings, B., Herrero, A., de Koter, A., Menon, A., Patrick, L., Puls, J., Renzo, M., Sander, A. A. C., Schneider, F. R. N., Sen, K., Shenar, T., Simón-Días, S., Tauris, T. M., Tramper, F., Vink, J. S., and Xu, X.-T. Properties of ob star-black hole systems derived from detailed binary evolution models. *Astronomy & Astrophysics*, 638:A39, 2020.

[15] E. Laplace, Y. Götberg, S. E. de Mink, S. Justham, and R. Farmer. The expansion of stripped-envelope stars: Consequences for supernovae and gravitational-wave progenitors. *Astronomy & Astrophysics*, 637:A6, May 2020.

[16] Klencki, Jakub, Nelemans, Gijs, Istrate, Alina G., and Chruslinska, Martyna. It has to be cool: Supergiant progenitors of binary black hole mergers from common-envelope evolution. *Astronomy & Astrophysics*, 645:A54, 2021.

[17] Jakub Klencki, Alina Istrate, Gijs Nelemans, and Onno Pols. Partial-envelope stripping and nuclear-timescale mass transfer from evolved supergiants at low metallicity. *Astronomy & Astrophysics*, 662:A56, jun 2022.

[18] K. Sen, N. Langer, P. Marchant, A. Menon, S. E. de Mink, A. Schootemeijer, C. Schürmann, L. Mahy, B. Hastings, K. Nathaniel, H. Sana, C. Wang, and X. T. Xu. Detailed models of interacting short-period massive binary stars. *Astronomy & Astrophysics*, 659:A98, mar 2022.

[19] Adam Burrows, Joshua C. Dolence, and Jeremiah W. Murphy. An Investigation into the Character of Pre-explosion Core-collapse Supernova Shock Motion. *The Astrophysical Journal*, 759(1):5, November 2012.

[20] Hans-Thomas Janka. Explosion Mechanisms of Core-Collapse Supernovae. *Annual Review of Nuclear and Particle Science*, 62(1):407–451, November 2012.

[21] Hans-Thomas Janka, Florian Hanke, Lorenz Hüdepohl, Andreas Marek, Bernhard Müller, and Martin Obergaulinger. Core-collapse supernovae: Reflections and directions. *Progress of Theoretical and Experimental Physics*, 2012(1):01A309, 12 2012.

[22] Eric J. Lentz, Stephen W. Bruenn, W. Raphael Hix, Anthony Mezzacappa, O. E. Bronson Messer, Eirik Endeve, John M. Blondin, J. Austin Harris, Pedro Marronetti, and Konstantin N. Yakunin. Three-dimensional Core-collapse Supernova Simulated Using a 15 M $_\odot$ Progenitor. *The Astrophysical Journal, Letters*, 807(2):L31, July 2015.

[23] Tobias Melson, Hans-Thomas Janka, and Andreas Marek. Neutrino-driven Supernova of a Low-mass Iron-core Progenitor Boosted by Three-dimensional Turbulent Convection. *The Astrophysical Journal, Letters*, 801(2):L24, March 2015.

[24] Tobias Melson, Hans-Thomas Janka, Robert Bollig, Florian Hanke, Andreas Marek, and Bernhard Müller. Neutrino-driven Explosion of a 20 Solar-mass Star in Three Dimensions Enabled by Strange-quark Contributions to Neutrino-Nucleon Scattering. *The Astrophysical Journal, Letters*, 808(2):L42, August 2015.

[25] Alexander Summa, Florian Hanke, Hans-Thomas Janka, Tobias Melson, Andreas Marek, and Bernhard Müller. PROGENITOR-DEPENDENT EXPLOSION DYNAMICS IN SELF-CONSISTENT, AXISYMMETRIC SIMULATIONS OF NEUTRINO-DRIVEN CORE-COLLAPSE SUPERNOVAE. *The Astrophysical Journal*, 825(1):6, jun 2016.

[26] Yudai Suwa, Kei Kotake, Tomoya Takiwaki, Stuart C. Whitehouse, Matthias LiebendÃ-rfer, and Katsuhiko Sato. Explosion Geometry of a Rotating 13M$_\odot$ Star Driven by the SASI-Aided Neutrino-Heating Supernova Mechanism. *Publications of the Astronomical Society of Japan*, 62(6):L49–L53, December 2010.

[27] Bernhard Müller, Alexander Heger, David Liptai, and Joshua B. Cameron. A simple approach to the supernova progenitor-explosion connection. *Monthly Notices of the Royal Astronomical Society*, 460(1):742–764, July 2016.

[28] R. Abbott, T. D. Abbott, S. Abraham, F. Acernese, K. Ackley, C. Adams, R. X. Adhikari, V. B. Adya, C. Affeldt, M. Agathos, K. Agatsuma, N. Aggarwal, O. D. Aguiar, A. Aich, L. Aiello, A. Ain, P. Ajith, S. Akcay, G. Allen, A. Allocca, P. A. Altin, A. Amato, S. Anand, A. Ananyeva, S. B. Anderson, W. G. Anderson, S. V. Angelova, S. Ansoldi, S. Antier, S. Appert, K. Arai, M. C. Araya, J. S. Areeda, M. Arène, N. Arnaud, S. M. Aronson, K. G. Arun, Y. Asali, S. Ascenzi, G. Ashton, S. M. Aston, P. Astone, F. Aubin, P. Aufmuth, K. AultONeal, C. Austin, V. Avendano, S. Babak, P. Bacon, F. Badaracco, M. K. M. Bader, S. Bae, A. M. Baer, J. Baird, F. Baldaccini, G. Ballardin, S. W. Ballmer, A. Bals, A. Balsamo, G. Baltus, S. Banagiri, D. Bankar, R. S. Bankar, J. C. Barayoga, C. Barbieri, B. C. Barish, D. Barker, K. Barkett, P. Barneo, F. Barone, B. Barr, L. Barsotti, M. Barsuglia, D. Barta, J. Bartlett, I. Bartos, R. Bassiri, A. Basti, M. Bawaj, J. C. Bayley, M. Bazzan, B. Bécsy, M. Bejger, I. Belahcene, A. S. Bell, D. Beniwal, M. G. Benjamin, R. Benkel, J. D. Bentley, F. Bergamin, B. K. Berger, G. Bergmann, S. Bernuzzi, C. P. L. Berry, D. Bersanetti, A. Bertolini, J. Betzwieser, R. Bhandare,

A. V. Bhandari, J. Bidler, E. Biggs, I. A. Bilenko, G. Billingsley, R. Birney, O. Birnholtz, S. Biscans, M. Bischi, S. Biscoveanu, A. Bisht, G. Bissenbayeva, M. Bitossi, M. A. Bizouard, J. K. Blackburn, J. Blackman, C. D. Blair, D. G. Blair, R. M. Blair, F. Bobba, N. Bode, M. Boer, Y. Boetzel, G. Bogaert, F. Bondu, E. Bonilla, R. Bonnand, P. Booker, B. A. Boom, R. Bork, V. Boschi, S. Bose, V. Bossilkov, J. Bosveld, Y. Bouffanais, A. Bozzi, C. Bradaschia, P. R. Brady, A. Bramley, M. Branchesi, J. E. Brau, M. Breschi, T. Briant, J. H. Briggs, F. Brighenti, A. Brillet, M. Brinkmann, R. Brito, P. Brockill, A. F. Brooks, J. Brooks, D. D. Brown, S. Brunett, G. Bruno, R. Bruntz, A. Buikema, T. Bulik, H. J. Bulten, A. Buonanno, D. Buskulic, R. L. Byer, M. Cabero, L. Cadonati, G. Cagnoli, C. Cahillane, J. Calderón Bustillo, J. D. Callaghan, T. A. Callister, E. Calloni, J. B. Camp, M. Canepa, K. C. Cannon, H. Cao, J. Cao, G. Carapella, F. Carbognani, S. Caride, M. F. Carney, G. Carullo, J. Casanueva Diaz, C. Casentini, J. Castañeda, S. Caudill, M. Cavaglià, F. Cavalier, R. Cavalieri, G. Cella, P. Cerdá-Durán, E. Cesarini, O. Chaibi, K. Chakravarti, C. Chan, M. Chan, S. Chao, P. Charlton, E. A. Chase, E. Chassande-Mottin, D. Chatterjee, M. Chaturvedi, K. Chatziioannou, H. Y. Chen, X. Chen, Y. Chen, H. P. Cheng, C. K. Cheong, H. Y. Chia, F. Chiadini, R. Chierici, A. Chincarini, A. Chiummo, G. Cho, H. S. Cho, M. Cho, N. Christensen, Q. Chu, S. Chua, K. W. Chung, S. Chung, G. Ciani, P. Ciecielag, M. Cieślar, A. A. Ciobanu, R. Ciolfi, F. Cipriano, A. Cirone, F. Clara, J. A. Clark, P. Clearwater, S. Clesse, F. Cleva, E. Coccia, P. F. Cohadon, D. Cohen, M. Colleoni, C. G. Collette, C. Collins, M. Colpi, Jr. Constancio, M., L. Conti, S. J. Cooper, P. Corban, T. R. Corbitt, I. Cordero-Carrión, S. Corezzi, K. R. Corley, N. Cornish, D. Corre, A. Corsi, S. Cortese, C. A. Costa, R. Cotesta, M. W. Coughlin, S. B. Coughlin, J. P. Coulon, S. T. Countryman, P. Couvares, P. B. Covas, D. M. Coward, M. J. Cowart, D. C. Coyne, R. Coyne, J. D. E. Creighton, T. D. Creighton, J. Cripe, M. Croquette, S. G. Crowder, J. R. Cudell, T. J. Cullen, A. Cumming, R. Cummings, L. Cunningham, E. Cuoco, M. Curylo, T. Dal Canton, G. Dálya, A. Dana, L. M. Daneshgaran-Bajastani, B. D'Angelo, S. L. Danilishin, S. D'Antonio, K. Danzmann, C. Darsow-Fromm, A. Dasgupta, L. E. H. Datrier, V. Dattilo, I. Dave, M. Davier, G. S. Davies, D. Davis, E. J. Daw, D. DeBra, M. Deenadayalan, J. Degallaix, M. De Laurentis, S. Deléglise, M. Delfavero, N. De Lillo, W. Del Pozzo, L. M. DeMarchi, V. D'Emilio, N. Demos, T. Dent, R. De Pietri, R. De Rosa, C. De Rossi, R. DeSalvo, O. de Varona, S. Dhurandhar, M. C. Díaz, Jr. Diaz-Ortiz, M., T. Dietrich, L. Di Fiore, C. Di Fronzo, C. Di Giorgio, F. Di Giovanni, M. Di Giovanni, T. Di Girolamo, A. Di Lieto, B. Ding, S. Di Pace, I. Di Palma, F. Di Renzo, A. K. Divakarla, A. Dmitriev, Z. Doctor, F. Donovan, K. L. Dooley, S. Doravari, I. Dorrington, T. P. Downes, M. Drago, J. C. Driggers, Z. Du, J. G. Ducoin, P. Dupej, O. Durante, D. D'Urso, S. E. Dwyer, P. J. Easter, G. Eddolls, B. Edelman, T. B. Edo, O. Edy, A. Effler, P. Ehrens, J. Eichholz, S. S. Eikenberry, M. Eisenmann, R. A. Eisenstein, A. Ejlli, L. Errico, R. C. Essick, H. Estelles, D. Estevez, Z. B. Etienne, T. Etzel, M. Evans, T. M. Evans, B. E. Ewing, V. Fafone, S. Fairhurst, X. Fan, S. Farinon, B. Farr, W. M. Farr, E. J. Fauchon-Jones, M. Favata, M. Fays, M. Fazio, J. Feicht, M. M. Fejer, F. Feng, E. Fenyvesi, D. L. Ferguson, A. Fernandez-Galiana, I. Ferrante, E. C. Ferreira, T. A. Ferreira, F. Fidecaro, I. Fiori, D. Fiorucci, M. Fishbach, R. P. Fisher, R. Fittipaldi, M. Fitz-Axen, V. Fiumara, R. Flaminio, E. Floden, E. Flynn, H. Fong, J. A. Font, P. W. F. Forsyth, J. D. Fournier, S. Frasca, F. Frasconi, Z. Frei, A. Freise, R. Frey, V. Frey, P. Fritschel, V. V. Frolov, G. Fronzè, P. Fulda, M. Fyffe, H. A. Gabbard, B. U. Gadre, S. M. Gaebel, J. R. Gair, S. Galaudage, D. Ganapathy, A. Ganguly, S. G. Gaonkar, C. García-Quirós, F. Garufi, B. Gateley, S. Gaudio, V. Gayathri, G. Gemme, E. Genin, A. Gennai, D. George, J. George, L. Gergely, S. Ghonge, Abhirup Ghosh, Archisman Ghosh, S. Ghosh, B. Giacomazzo, J. A. Giaime, K. D. Giardina, D. R. Gibson, C. Gier, K. Gill, J. Glanzer, J. Gniesmer, P. Godwin, E. Goetz, R. Goetz, N. Gohlke, B. Goncharov, G. González, A. Gopakumar, S. E. Gossan, M. Gosselin, R. Gouaty, B. Grace, A. Grado, M. Granata, A. Grant, S. Gras, P. Grassia, C. Gray, R. Gray, G. Greco, A. C. Green, R. Green, E. M. Gretarsson, H. L. Griggs, G. Grignani, A. Grimaldi, S. J. Grimm, H. Grote, S. Grunewald, P. Gruning, G. M. Guidi, A. R. Guimaraes, G. Guixé, H. K. Gulati, Y. Guo, A. Gupta, Anchal Gupta, P. Gupta, E. K. Gustafson, R. Gustafson, L. Haegel, O. Halim, E. D. Hall, E. Z. Hamilton, G. Hammond, M. Haney, M. M. Hanke, J. Hanks, C. Hanna, M. D. Hannam, O. A. Hannuksela, T. J. Hansen, J. Hanson, T. Harder, T. Hardwick, K. Haris, J. Harms, G. M. Harry, I. W. Harry, R. K. Hasskew, C. J. Haster, K. Haughian, F. J. Hayes, J. Healy, A. Heidmann, M. C. Heintze, J. Heinze, H. Heitmann, F. Hellman, P. Hello, G. Hemming, M. Hendry, I. S. Heng, E. Hennes, J. Hennig, M. Heurs, S. Hild, T. Hinderer, S. Y. Hoback, S. Hochheim, E. Hofgard, D. Hofman, A. M. Holgado, N. A. Holland, K. Holt, D. E. Holz, P. Hopkins, C. Horst, J. Hough, E. J. Howell, C. G. Hoy, Y. Huang, M. T. Hübner, E. A. Huerta, D. Huet, B. Hughey, V. Hui, S. Husa, S. H. Huttner, R. Huxford, T. Huynh-Dinh, B. Idzkowski, A. Iess, H. Inchauspe, C. Ingram, G. Intini, J. M. Isac, M. Isi, B. R. Iyer, T. Jacqmin, S. J. Jadhav, S. P. Jadhav, A. L. James, K. Jani, N. N. Janthalur, P. Jaranowski, D. Jariwala, R. Jaume, A. C. Jenkins, J. Jiang, G. R. Johns, N. K. Johnson-McDaniel, A. W. Jones, D. I. Jones, J. D. Jones, P. Jones, R. Jones, R. J. G. Jonker, L. Ju, J. Junker, C. V. Kalaghatgi, V. Kalogera, B. Kamai, S. Kandhasamy, G. Kang, J. B. Kanner, S. J. Kapadia, S. Karki, R. Kashyap, M. Kasprzack, W. Kastaun, S. Katsanevas, E. Katsavounidis, W. Katzman, S. Kaufer, K. Kawabe, F. Kéfélian, D. Keitel, A. Keivani, R. Kennedy, J. S. Key, S. Khadka, F. Y. Khalili, I. Khan, S. Khan, Z. A. Khan, E. A. Khazanov, N. Khetan, M. Khursheed, N. Kijbunchoo, Chunglee Kim, G. J. Kim, J. C. Kim, K. Kim, W. Kim, W. S. Kim, Y. M. Kim, C. Kimball, P. J. King, M. Kinley-Hanlon, R. Kirchhoff, J. S. Kissel, L. Kleybolte, S. Klimenko, T. D. Knowles, E. Knyazev, P. Koch, S. M. Koehlenbeck, G. Koekoek, S. Koley, V. Kondrashov, A. Kontos, N. Koper, M. Korobko, W. Z. Korth, M. Kovalam, D. B. Kozak, V. Kringel, N. V. Krishnendu, A. Królak, N. Krupinski, G. Kuehn, A. Kumar, P. Kumar, Rahul Kumar, Rakesh Kumar, S. Kumar, L. Kuo, A. Kutynia, B. D. Lackey, D. Laghi, E. Lalande, T. L. Lam, A. Lamberts, M. Landry, P. Landry, B. B. Lane, R. N. Lang, J. Lange, B. Lantz, R. K. Lanza,

I. La Rosa, A. Lartaux-Vollard, P. D. Lasky, M. Laxen, A. Lazzarini, C. Lazzaro, P. Leaci, S. Leavey, Y. K. Lecoeuche, C. H. Lee, H. M. Lee, H. W. Lee, J. Lee, K. Lee, J. Lehmann, N. Leroy, N. Letendre, Y. Levin, A. K. Y. Li, J. Li, K. li, T. G. F. Li, X. Li, F. Linde, S. D. Linker, J. N. Linley, T. B. Littenberg, J. Liu, X. Liu, M. Llorens-Monteagudo, R. K. L. Lo, A. Lockwood, L. T. London, A. Longo, M. Lorenzini, V. Loriette, M. Lormand, G. Losurdo, J. D. Lough, C. O. Lousto, G. Lovelace, H. Lück, D. Lumaca, A. P. Lundgren, Y. Ma, R. Macas, S. Macfoy, M. MacInnis, D. M. Macleod, I. A. O. MacMillan, A. Macquet, I. Magaña Hernandez, F. Magaña-Sandoval, R. M. Magee, E. Majorana, I. Maksimovic, A. Malik, N. Man, V. Mandic, V. Mangano, G. L. Mansell, M. Manske, M. Mantovani, M. Mapelli, F. Marchesoni, F. Marion, S. Márka, Z. Márka, C. Markakis, A. S. Markosyan, A. Markowitz, E. Maros, A. Marquina, S. Marsat, F. Martelli, I. W. Martin, R. M. Martin, V. Martinez, D. V. Martynov, H. Masalehdan, K. Mason, E. Massera, A. Masserot, T. J. Massinger, M. Masso-Reid, S. Mastrogiovanni, A. Matas, F. Matichard, N. Mavalvala, E. Maynard, J. J. McCann, R. McCarthy, D. E. McClelland, S. McCormick, L. McCuller, S. C. McGuire, C. McIsaac, J. McIver, D. J. McManus, T. McRae, S. T. McWilliams, D. Meacher, G. D. Meadors, M. Mehmet, A. K. Mehta, E. Mejuto Villa, A. Melatos, G. Mendell, R. A. Mercer, L. Mereni, K. Merfeld, E. L. Merilh, J. D. Merritt, M. Merzougui, S. Meshkov, C. Messenger, C. Messick, R. Metzdorff, P. M. Meyers, F. Meylahn, A. Mhaske, A. Miani, H. Miao, I. Michaloliakos, C. Michel, H. Middleton, L. Milano, A. L. Miller, M. Millhouse, J. C. Mills, E. Milotti, M. C. Milovich-Goff, O. Minazzoli, Y. Minenkov, A. Mishkin, C. Mishra, T. Mistry, S. Mitra, V. P. Mitrofanov, G. Mitselmakher, R. Mittleman, G. Mo, K. Mogushi, S. R. P. Mohapatra, S. R. Mohite, M. Molina-Ruiz, M. Mondin, M. Montani, C. J. Moore, D. Moraru, F. Morawski, G. Moreno, S. Morisaki, B. Mours, C. M. Mow-Lowry, S. Mozzon, F. Muciaccia, Arunava Mukherjee, D. Mukherjee, S. Mukherjee, Subroto Mukherjee, N. Mukund, A. Mullavey, J. Munch, E. A. Muñiz, P. G. Murray, A. Nagar, I. Nardecchia, L. Naticchioni, R. K. Nayak, B. F. Neil, J. Neilson, G. Nelemans, T. J. N. Nelson, M. Nery, A. Neunzert, K. Y. Ng, S. Ng, C. Nguyen, P. Nguyen, D. Nichols, S. A. Nichols, S. Nissanke, F. Nocera, M. Noh, C. North, D. Nothard, L. K. Nuttall, J. Oberling, B. D. O'Brien, G. Oganesyan, G. H. Ogin, J. J. Oh, S. H. Oh, F. Ohme, H. Ohta, M. A. Okada, M. Oliver, C. Olivetto, P. Oppermann, Richard J. Oram, B. O'Reilly, R. G. Ormiston, L. F. Ortega, R. O'Shaughnessy, S. Ossokine, C. Osthelder, D. J. Ottaway, H. Overmier, B. J. Owen, A. E. Pace, G. Pagano, M. A. Page, G. Pagliaroli, A. Pai, S. A. Pai, J. R. Palamos, O. Palashov, C. Palomba, H. Pan, P. K. Panda, P. T. H. Pang, C. Pankow, F. Pannarale, B. C. Pant, F. Paoletti, A. Paoli, A. Parida, W. Parker, D. Pascucci, A. Pasqualetti, R. Passaquieti, D. Passuello, B. Patricelli, E. Payne, B. L. Pearlstone, T. C. Pechsiri, A. J. Pedersen, M. Pedraza, A. Pele, S. Penn, A. Perego, C. J. Perez, C. Périgois, A. Perreca, S. Perriès, J. Petermann, H. P. Pfeiffer, M. Phelps, K. S. Phukon, O. J. Piccinni, M. Pichot, M. Piendibene, F. Piergiovanni, V. Pierro, G. Pillant, L. Pinard, I. M. Pinto, K. Piotrzkowski, M. Pirello, M. Pitkin, W. Plastino, R. Poggiani, D. Y. T. Pong, S. Ponrathnam, P. Popolizio, E. K. Porter, J. Powell, A. K. Prajapati, K. Prasai, R. Prasanna, G. Pratten, T. Prestegard, M. Principe, G. A. Prodi, L. Prokhorov, M. Punturo, P. Puppo, M. Pürrer, H. Qi, V. Quetschke, P. J. Quinonez, F. J. Raab, G. Raaijmakers, H. Radkins, N. Radulesco, P. Raffai, H. Rafferty, S. Raja, C. Rajan, B. Rajbhandari, M. Rakhmanov, K. E. Ramirez, A. Ramos-Buades, Javed Rana, K. Rao, P. Rapagnani, V. Raymond, M. Razzano, J. Read, T. Regimbau, L. Rei, S. Reid, D. H. Reitze, P. Rettegno, F. Ricci, C. J. Richardson, J. W. Richardson, P. M. Ricker, G. Riemenschneider, K. Riles, M. Rizzo, N. A. Robertson, F. Robinet, A. Rocchi, R. D. Rodriguez-Soto, L. Rolland, J. G. Rollins, V. J. Roma, M. Romanelli, R. Romano, C. L. Romel, I. M. Romero-Shaw, J. H. Romie, C. A. Rose, D. Rose, K. Rose, D. Rosińska, S. G. Rosofsky, M. P. Ross, S. Rowan, S. J. Rowlinson, P. K. Roy, Santosh Roy, Soumen Roy, P. Ruggi, G. Rutins, K. Ryan, S. Sachdev, T. Sadecki, M. Sakellariadou, O. S. Salafia, L. Salconi, M. Saleem, F. Salemi, A. Samajdar, E. J. Sanchez, L. E. Sanchez, N. Sanchis-Gual, J. R. Sanders, K. A. Santiago, E. Santos, N. Sarin, B. Sassolas, B. S. Sathyaprakash, O. Sauter, R. L. Savage, V. Savant, D. Sawant, S. Sayah, D. Schaetzl, P. Schale, M. Scheel, J. Scheuer, P. Schmidt, R. Schnabel, R. M. S. Schofield, A. Schönbeck, E. Schreiber, B. W. Schulte, B. F. Schutz, O. Schwarm, E. Schwartz, J. Scott, S. M. Scott, E. Seidel, D. Sellers, A. S. Sengupta, N. Sennett, D. Sentenac, V. Sequino, A. Sergeev, Y. Setyawati, D. A. Shaddock, T. Shaffer, M. S. Shahriar, A. Sharma, P. Sharma, P. Shawhan, H. Shen, M. Shikauchi, R. Shink, D. H. Shoemaker, D. M. Shoemaker, K. Shukla, S. ShyamSundar, K. Siellez, M. Sieniawska, D. Sigg, L. P. Singer, D. Singh, N. Singh, A. Singha, A. Singhal, A. M. Sintes, V. Sipala, V. Skliris, B. J. J. Slagmolen, T. J. Slaven-Blair, J. Smetana, J. R. Smith, R. J. E. Smith, S. Somala, E. J. Son, S. Soni, B. Sorazu, V. Sordini, F. Sorrentino, T. Souradeep, E. Sowell, A. P. Spencer, M. Spera, A. K. Srivastava, V. Srivastava, K. Staats, C. Stachie, M. Standke, D. A. Steer, J. Steinhoff, M. Steinke, J. Steinlechner, S. Steinlechner, D. Steinmeyer, S. Stevenson, D. Stocks, D. J. Stops, M. Stover, K. A. Strain, G. Stratta, A. Strunk, R. Sturani, A. L. Stuver, S. Sudhagar, V. Sudhir, T. Z. Summerscales, L. Sun, S. Sunil, A. Sur, J. Suresh, P. J. Sutton, B. L. Swinkels, M. J. Szczepańczyk, M. Tacca, S. C. Tait, C. Talbot, A. J. Tanasijczuk, D. B. Tanner, D. Tao, M. Tápai, A. Tapia, E. N. Tapia San Martin, J. D. Tasson, R. Taylor, R. Tenorio, L. Terkowski, M. P. Thirugnanasambandam, M. Thomas, P. Thomas, J. E. Thompson, S. R. Thondapu, K. A. Thorne, E. Thrane, C. L. Tinsman, T. R. Saravanan, Shubhanshu Tiwari, S. Tiwari, V. Tiwari, K. Toland, M. Tonelli, Z. Tornasi, A. Torres-Forné, C. I. Torrie, I. Tosta e Melo, D. Töyrä, E. A. Trail, F. Travasso, G. Traylor, M. C. Tringali, A. Tripathee, A. Trovato, R. J. Trudeau, K. W. Tsang, M. Tse, R. Tso, L. Tsukada, D. Tsuna, T. Tsutsui, M. Turconi, A. S. Ubhi, K. Ueno, D. Ugolini, C. S. Unnikrishnan, A. L. Urban, S. A. Usman, A. C. Utina, H. Vahlbruch, G. Vajente, G. Valdes, M. Valentini, N. van Bakel, M. van Beuzekom, J. F. J. van den Brand, C. Van Den Broeck, D. C. Vander-Hyde, L. van der Schaaf, J. V. Van Heijningen, A. A. van Veggel, M. Vardaro, V. Varma, S. Vass, M. Vasúth, A. Vecchio,

G. Vedovato, J. Veitch, P. J. Veitch, K. Venkateswara, G. Venugopalan, D. Verkindt, D. Veske, F. Vetrano, A. Viceré, A. D. Viets, S. Vinciguerra, D. J. Vine, J. Y. Vinet, S. Vitale, Francisco Hernandez Vivanco, T. Vo, H. Vocca, C. Vorvick, S. P. Vyatchanin, A. R. Wade, L. E. Wade, M. Wade, R. Walet, M. Walker, G. S. Wallace, L. Wallace, S. Walsh, J. Z. Wang, S. Wang, W. H. Wang, R. L. Ward, Z. A. Warden, J. Warner, M. Was, J. Watchi, B. Weaver, L. W. Wei, M. Weinert, A. J. Weinstein, R. Weiss, F. Wellmann, L. Wen, P. Weßels, J. W. Westhouse, K. Wette, J. T. Whelan, B. F. Whiting, C. Whittle, D. M. Wilken, D. Williams, J. L. Willis, B. Willke, W. Winkler, C. C. Wipf, H. Wittel, G. Woan, J. Woehler, J. K. Wofford, C. Wong, J. L. Wright, D. S. Wu, D. M. Wysocki, L. Xiao, H. Yamamoto, L. Yang, Y. Yang, Z. Yang, M. J. Yap, M. Yazback, D. W. Yeeles, Hang Yu, Haocun Yu, S. H. R. Yuen, A. K. Zadrożny, A. Zadrożny, M. Zanolin, T. Zelenova, J. P. Zendri, M. Zevin, J. Zhang, L. Zhang, T. Zhang, C. Zhao, G. Zhao, M. Zhou, Z. Zhou, X. J. Zhu, A. B. Zimmerman, M. E. Zucker, J. Zweizig, LIGO Scientific Collaboration, and Virgo Collaboration. GW190814: Gravitational Waves from the Coalescence of a 23 Solar Mass Black Hole with a 2.6 Solar Mass Compact Object. *The Astrophysical Journal, Letters*, 896(2):L44, June 2020.

[29] B. Paxton, L. Bildsten, A. Dotter, F. Herwig, P. Lesaffre, and F. Timmes. Modules for Experiments in Stellar Astrophysics (MESA). *The Astrophysical Journal, Supplement*, 192:3, jan 2011.

[30] B. Paxton, M. Cantiello, P. Arras, L. Bildsten, E. F. Brown, A. Dotter, C. Mankovich, M. H. Montgomery, D. Stello, F. X. Timmes, and R. Townsend. Modules for Experiments in Stellar Astrophysics (MESA): Planets, Oscillations, Rotation, and Massive Stars. *The Astrophysical Journal, Supplement*, 208:4, sep 2013.

[31] B. Paxton, P. Marchant, J. Schwab, E. B. Bauer, L. Bildsten, M. Cantiello, L. Dessart, R. Farmer, H. Hu, N. Langer, R. H. D. Townsend, D. M. Townsley, and F. X. Timmes. Modules for Experiments in Stellar Astrophysics (MESA): Binaries, Pulsations, and Explosions. *The Astrophysical Journal, Supplement*, 220:15, sep 2015.

[32] B. Paxton, J. Schwab, E. B. Bauer, L. Bildsten, S. Blinnikov, P. Duffell, R. Farmer, J. A. Goldberg, P. Marchant, E. Sorokina, A. Thoul, R. H. D. Townsend, and F. X. Timmes. Modules for Experiments in Stellar Astrophysics (MESA): Convective Boundaries, Element Diffusion, and Massive Star Explosions. *The Astrophysical Journal, Supplement*, 234:34, feb 2018.

[33] Bill Paxton, R. Smolec, Josiah Schwab, A. Gautschy, Lars Bildsten, Matteo Cantiello, Aaron Dotter, R. Farmer, Jared A. Goldberg, Adam S. Jermyn, S. M. Kanbur, Pablo Marchant, Anne Thoul, Richard H. D. Townsend, William M. Wolf, Michael Zhang, and F. X. Timmes. Modules for Experiments in Stellar Astrophysics (MESA): Pulsating Variable Stars, Rotation, Convective Boundaries, and Energy Conservation. *The Astrophysical Journal, Supplement*, 243(1):10, Jul 2019.

[34] David R. Aguilera-Dena, Norbert Langer, John Antoniadis, Daniel Pauli, Luc Dessart, Alejandro Vigna-Gómez, Götz Gräfener, and Sung-Chul Yoon. Stripped-envelope stars in different metallicity environments. I. Evolutionary phases, classification, and populations. *Astronomy & Astrophysics*, 661:A60, May 2022.

[35] David R. Aguilera-Dena, Bernhard Müller, John Antoniadis, Norbert Langer, Luc Dessart, Alejandro Vigna-Gómez, and Sung-Chul Yoon. Stripped-envelope stars in different metallicity environments. II. Type I supernovae and compact remnants. *Astronomy & Astrophysics*, 671:A134, March 2023.

[36] S. E. Woosley and Alexander Heger. Erratum: "Long Gamma-Ray Transients from Collapsars". *The Astrophysical Journal*, 806(1):145, June 2015.

[37] Bernhard Müller and Hans-Thomas Janka. A New Multi-dimensional General Relativistic Neutrino Hydrodynamics Code for Core-collapse Supernovae. IV. The Neutrino Signal. *The Astrophysical Journal*, 788(1):82, June 2014.

[38] James M. Lattimer and A. Yahil. Analysis of the Neutrino Events from Supernova 1987A. *The Astrophysical Journal*, 340:426, May 1989.

[39] J. M. Lattimer and M. Prakash. Neutron Star Structure and the Equation of State. *The Astrophysical Journal*, 550(1):426–442, March 2001.

[40] B. Müller and H. Th. Janka. Non-radial instabilities and progenitor asphericities in core-collapse supernovae. *Monthly Notices of the Royal Astronomical Society*, 448(3):2141–2174, April 2015.

[41] B. Müller. The dynamics of neutrino-driven supernova explosions after shock revival in 2D and 3D. *Monthly Notices of the Royal Astronomical Society*, 453(1):287–310, October 2015.

[42] Kitaura, F. S., Janka, H.-Th., and Hillebrandt, W. Explosions of o-ne-mg cores, the crab supernova, and subluminous type ii-p supernovae. *Astronomy & Astrophysics*, 450(1):345–350, 2006.

[43] Bernhard Müller, Hans-Thomas Janka, and Alexander Heger. New Two-dimensional Models of Supernova Explosions by the Neutrino-heating Mechanism: Evidence for Different Instability Regimes in Collapsing Stellar Cores. *The Astrophysical Journal*, 761(1):72, December 2012.

[44] Stephen W. Bruenn, Anthony Mezzacappa, W. Raphael Hix, Eric J. Lentz, O. E. Bronson Messer, Eric J. Lingerfelt, John M. Blondin, Eirik Endeve, Pedro Marronetti, and Konstantin N. Yakunin. AXISYMMETRIC AB INITIO CORE-COLLAPSE SUPERNOVA SIMULATIONS OF 12-25 $M_\odot$ STARS. *The Astrophysical Journal Letters*, 767(1):L6, mar 2013.

[45] Evan P. O'Connor and Sean M. Couch. Two-dimensional core-collapse supernova explosions aided by general relativity with multidimensional neutrino transport. *The Astrophysical Journal*, 854(1):63, feb 2018.

[46] Tomoya Takiwaki, Kei Kotake, and Yudai Suwa. Three-dimensional Hydrodynamic Core-collapse Supernova Simulations for an 11.2 $M_\odot$ Star with Spectral Neutrino Transport. *The Astrophysical Journal*, 749(2):98, April 2012.

[47] A. Marek and H. Th. Janka. Delayed Neutrino-Driven Supernova Explosions Aided by the Standing Accretion-Shock Instability. *The Astrophysical Journal*, 694(1):664–696, March 2009.

[48] Christopher D. Matzner and Christopher F. McKee. The expulsion of stellar envelopes in core-collapse supernovae. *The Astrophysical Journal*, 510(1):379, jan 1999.

[49] L. Scheck, K. Kifonidis, H. Th. Janka, and E. Müller. Multidimensional supernova simulations with approximative neutrino transport. I. Neutron star kicks and the anisotropy of neutrino-driven explosions in two spatial dimensions. *Astronomy & Astrophysics*, 457(3):963–986, October 2006.

[50] Bernhard Müller, Hans-Thomas Janka, and Andreas Marek. A New Multi-dimensional General Relativistic Neutrino Hydrodynamics Code for Core-collapse Supernovae. II. Relativistic Explosion Models of Core-collapse Supernovae. *The Astrophysical Journal*, 756(1):84, September 2012.

[51] M. Rampp and H. T. Janka. Radiation hydrodynamics with neutrinos. Variable Eddington factor method for core-collapse supernova simulations. *Astronomy & Astrophysics*, 396:361–392, December 2002.

[52] Christian Iliadis. *Nuclear Physics of Stars*. Wiley, February 2007.

[53] Stuart L. Shapiro and Saul A. Teukolsky. *Black holes, white dwarfs and neutron stars. The physics of compact objects*. 1983.

[54] Lorenz Hüdepohl. *Neutrinos from the Formation, Cooling, and Black Hole Collapse of Neutron Stars*. PhD thesis, Technische Universität München, 2014.

[55] Janka, H.-Th., Müller, B., Kitaura, F. S., and Buras, R. Dynamics of shock propagation and nucleosynthesis conditions in o-ne-mg core supernovae. *Astronomy & Astrophysics*, 485(1):199–208, 2008.

[56] Fabian R. N. Schneider, Philipp Podsiadlowski, and Eva Laplace. Bimodal Black Hole Mass Distribution and Chirp Masses of Binary Black Hole Mergers. *The Astrophysical Journal, Letters*, 950(2):L9, June 2023.

[57] E. E. Salpeter. Electrons Screening and Thermonuclear Reactions. *Australian Journal of Physics*, 7:373, September 1954.

[58] S. E. Woosley. The Evolution of Massive Helium Stars, Including Mass Loss. *The Astrophysical Journal*, 878(1):49, June 2019.

[59] Charles R. Harris, K. Jarrod Millman, Stéfan J. van der Walt, Ralf Gommers, Pauli Virtanen, David Cournapeau, Eric Wieser, Julian Taylor, Sebastian Berg, Nathaniel J. Smith, Robert Kern, Matti Picus, Stephan Hoyer, Marten H. van Kerkwijk, Matthew Brett, Allan Haldane, Jaime Fernández del Río, Mark Wiebe, Pearu Peterson, Pierre Gérard-Marchant, Kevin Sheppard, Tyler Reddy, Warren Weckesser, Hameer Abbasi, Christoph Gohlke, and Travis E. Oliphant. Array programming with NumPy. *Nature*, 585(7825):357–362, September 2020.

[60] F. Pedregosa, G. Varoquaux, A. Gramfort, V. Michel, B. Thirion, O. Grisel, M. Blondel, P. Prettenhofer, R. Weiss, V. Dubourg, J. Vanderplas, A. Passos, D. Cournapeau, M. Brucher, M. Perrot, and E. Duchesnay. Scikit-learn: Machine learning in Python. *Journal of Machine Learning Research*, 12:2825–2830, 2011.

[61] Ernst Wit, Edwin van den Heuvel, and Jan-Willem Romeijn. 'all models are wrong...': an introduction to model uncertainty. *Statistica Neerlandica*, 66(3):217–236, 2012.

[62] Keith M. Ashman, Christina M. Bird, and Stephen E. Zepf. Detecting Bimodality in Astronomical Datasets. *The Astrophysical Journal*, 108:2348, December 1994.

[63] Jarrod R. Hurley, Onno R. Pols, and Christopher A. Tout. Comprehensive analytic formulae for stellar evolution as a function of mass and metallicity. *Monthly Notices of the Royal Astronomical Society*, 315(3):543–569, July 2000.

[64] Ilya Mandel and Bernhard Müller. Simple recipes for compact remnant masses and natal kicks. *Monthly Notices of the Royal Astronomical Society*, 499(3):3214–3221, oct 2020.

[65] Jeff Riley, Poojan Agrawal, Jim W. Barrett, Kristan N. K. Boyett, Floor S. Broekgaarden, Debatri Chattopadhyay, Sebastian M. Gaebel, Fabian Gittins, Ryosuke Hirai, George Howitt, Stephen Justham, Lokesh Khandelwal, Floris Kummer, Mike Y. M. Lau, Ilya Mandel, Selma E. de Mink, Coenraad Neijssel, Tim Riley, Lieke van Son, Simon Stevenson, Alejandro Vigna-Gómez, Serena Vinciguerra, Tom Wagg, Reinhold Willcox, and Team Compas. Rapid Stellar and Binary Population Synthesis with COMPAS. *The Astrophysical Journal, Supplement*, 258(2):34, February 2022.